1   **Modeling impacts of ice-nucleating particles from marine aerosols on mixed-phase**

2   **orographic clouds during 2015 ACAPEX field campaign**

4   Yun Lin[1,2], Jiwen Fan[1,*], Pengfei Li[3,4], L. Ruby Leung[1], Paul J. DeMott[5], Lexie Goldberger[1],

5   Jennifer Comstock[1], Ying Liu[1], Jong-Hoon Jeong[1,2], Jason Tomlinson[1]

7   [1] Atmospheric Sciences and Global Change Division, Pacific Northwest National Laboratory,

8   Richland, WA 99352

9   [2] Joint Institute for Regional Earth System Science and Engineering (JIFRESSE), University of

10   California, Los Angeles (UCLA), Los Angeles, CA 90064

11   [3] College of Science and Technology, Hebei Agricultural University, Baoding, Hebei

12   14 071000, P.R. China

13   [4] Research Center for Air Pollution and Health; Key Laboratory of Environmental

14   Remediation and Ecological Health, Ministry of Education, College of Environment and

15   Resource Sciences, Zhejiang University, Hangzhou, Zhejiang 310058, P.R. China

16   [5] Department of Atmospheric Science, Colorado State University, Fort Collins, CO 80523, USA

18   Corresponding author: Jiwen Fan (jiwen.fan@pnnl.gov)

Abstract

A large fraction of annual precipitation over the western United States comes from wintertime orographic clouds associated with atmospheric rivers (ARs). Transported African and Asian dust and marine aerosols from the Pacific Ocean may act as ice-nucleating particles (INPs) to affect cloud and precipitation properties over the region. Here we explored the effects of INPs from marine aerosols on orographic mixed-phase clouds and precipitation at different AR stages for an AR event observed during the 2015 ACAPEX field campaign under low dust (< 0.02 cm^{-3}) conditions. Simulations were conducted using the chemistry version of the Weather Research and Forecasting model coupled with the spectral-bin microphysics at 1-km grid spacing, with ice nucleation connected with dust and marine aerosols. By comparing against airborne and ground-based observations, accounting for marine INP effects improves the simulation of AR-precipitation. The marine INPs enhance the formation of ice and snow, leading to less shallow warm clouds but more mixed-phase and deep clouds, as well as a large spillover effect of precipitation after AR landfall. The responses of cloud and precipitation to marine INPs vary with the AR stages with more significant effects before AR landfall and post-AR than after AR landfall, mainly because the moisture and temperature conditions change with the AR evolution. This work suggests weather and climate models need to consider the impacts of marine INPs since their contribution is notable under low dust conditions despite the much lower relative ice nucleation efficiency of marine INPs.

1 Introduction

Atmospheric river (AR) events have great impacts on atmospheric and hydrological processes in the western United States during winter. On a long-term average, AR storms contribute to 20–50% of California's precipitation totals (Dettinger et al., 2011). Understanding the factors influencing different types of precipitation (rain vs. snow) associated with ARs is crucial for planning and managing regional water resources and hydrologic hazards and improving atmospheric and hydrologic forecasting in the western United States. Rain and snow precipitation produced by orographic clouds over the Sierra Nevada Mountains is closely related to the partitioning between cloud liquid and ice phases, which can be largely modified by aerosol particles (Rosenfeld et al., 2013; Fan et al., 2014, 2017b). However, aerosol-orography-precipitation relationships are complicated, depending on aerosol properties, mountain geometry, cloud phase, temperature, humidity, and flow patterns as reviewed in Chouldhury et al. (2019).

Over the western United States, understanding the roles of aerosols, particularly those capable of initiating ice crystal formation in altering clouds and precipitation is still limited, which has motivated recent observational and modeling studies (Ault et al., 2011; Creamean et al., 2013, 2015; Rosenfeld et al., 2013; Fan et al., 2014, 2017b; Martin et al., 2019; Levin et al., 2019). While it has been found that long-range transported aerosols particularly dust particles as ice nucleating particles (INPs) influence clouds and precipitation in the mountainous western United States (Uno et al., 2009; Ault et al., 2011; Creamean et al., 2013), it is also clear from measurements that clouds occurring in and around ARs can also be influenced by INPs with apparent sources from the ocean (Levin et al., 2019).

Previous studies showed that INPs can increase total precipitation through the "seeder feeder" mechanism (Choularton and Perry, 1986; Creamean et al., 2013), in which ice crystals

65   that form in the upper portions of orographic clouds can collect droplets and grow to a larger size

66   as they fall through a supercooled liquid layer before reaching the ground. Fan et al. (2014,

67   2017b) found that INPs like dust particles can increase precipitation by enhancing riming and

68   deposition processes in mixed-phase orographic clouds, consistent with other studies (e.g.,

69   Muhlbauer and Lohmann, 2009; Xiao et al., 2015; Hazra et al., 2016; Yang et al., 2020). Fan et

70   al. (2017a) also noted that the relative importance of riming to deposition depends on the mixed-

71   phase cloud temperatures. Despite the importance of INPs in cloud formation and precipitation,

72   they typically have a low abundance and large variations in their nucleating characteristics,

73   especially in terms of the temperatures over which they initiate ice crystal formation (Kanji et al.,

74   2017; Levin et al., 2019). Hence, there is large uncertainty in evaluating INPs impacts on mixed-

75   phase and ice clouds as well as precipitation.

76   Dust and biological particles are known INPs. Biological particles can cause freezing at

77   temperatures as warm as −5 °C (Murray et al., 2012). During ARs, the long-range transport of

78   dust or biological particles is highly episodic (Creamean et al., 2013). Sea spray or marine

79   aerosols consisting of sea salt and marine organic carbon resulting from wave breaking and

80   bubble bursting at the ocean surface may also be a source of INPs (Burrows et al., 2013;

81   Vergara-Temprado et al., 2017; McCluskey et al., 2018b; Levin et al., 2019). Recently,

82   McCluskey et al. (2018a) derived an ice nucleation parameterization for INPs from sea spray

83   aerosols based on observations collected at a North Atlantic coastal site and its relation to the

84   marine aerosol surface area. Given the distinct physio-chemical characteristics and the different

85   ice-nucleating efficiency (magnitudes lower than mineral dust; McCluskey et al. 2018a), the

86   impact of marine INPs on cloud and precipitation could be very different from dust or biological

87   particles (DeMott et al., 2016; Kanji et al., 2017). However, studies of marine-sourced INP

88   effects on clouds and associated precipitation are limited (Kanji et al., 2017; Levin et al., 2019).

89   A few previous studies investigated the impacts of marine INPs on precipitation and radiation

90   with global climate models (Hoose et al., 2010; Burrows et al., 2013; Yun and Penner, 2013),

91   albeit without the advantage of direct data on their ice nucleation efficiencies. Further, a detailed,

92   process-level understanding of how marine INPs affect mixed-phase cloud processes and

93   precipitation is lacking.

94   Following the CalWater campaigns in 2009, 2011, 2014, an interagency sponsored study,

95   CalWater 2015, utilized a larger suite of instruments and measurement platforms to study ARs

96   and aerosol-cloud interactions in AR environments (Ralph et al., 2016). As part of CalWater

97   2015, the U.S. Department of Energy sponsored Atmospheric Radiation Measurement (ARM)

98   Cloud Aerosol Precipitation Experiment (ACAPEX) field campaign aimed specifically at

99   improving understanding and modeling of aerosol impacts on winter storms associated with

100   landfalling ARs (Leung et al., 2016). The ACAPEX campaign conducted intensive sampling of

101   clouds and aerosols using instruments on board the ARM Aerial Facility Gulfstream (G-1)

102   aircraft and ARM Mobile Facility on board the research vessel Ron Brown. These measurements

103   were made in conjunction with clouds and aerosols, meteorological, hydrological, and oceanic

104   measurements collected by instruments on three other aircraft and Ron Brown and at a coastal

105   surface station. Collectively, these data provide a unique opportunity to examine the complex

106   interactions among aerosols, orographic clouds, and ARs.

107   A major AR event spanning over 5 - 9 February 2015 occurred during the ACAPEX

108   campaign, producing heavy rainfall with some regions receiving up to 400 mm of total

109   precipitation during the event (Ralph et al., 2016; Cordeira et al., 2017). This AR event was

110   extensively sampled by the G-1 aircraft (Schmid et al., 2014) for characterizing aerosol and

111   cloud properties. During this event, marine aerosols were the main aerosol type and marine INPs

112   were dominant at cloud activation temperatures. Aerosol sampled by G-1 indicated that dust and

113   biological particles were rather scarce in and around ARs, which is in stark contrast to the

114   dominance of dust INPs during the AR events in the CalWater 2011 campaign (Levin et al.,

115   2019). Therefore, the AR event during the ACAPEX campaign provides a rather unique

116   opportunity to explore the role of marine aerosols in the orographic clouds and precipitation

117   associated with landfalling ARs in the western United States.

118   In our previous modeling studies (Fan et al., 2014, 2017b), we implemented an

119   immersion freezing parameterization for dust particles (DeMott et al. 2015) in a spectral-bin

120   microphysics (SBM) scheme to examine the long-range dust effects on AR-associated

121   orographic mixed-phase clouds and precipitation during CalWater 2011. With marine INPs

122   dominating in CalWater 2015/ACAPEX, in this study we implemented the recently developed

123   ice immersion nucleation parameterization for sea spray aerosols by McCluskey et al. (2018b) in

124   the SBM scheme. To explicitly simulate various aerosol types, different from Fan et al. (2014,

125   2017a) who prescribed aerosols based on observations, a chemistry version of the Weather

126   Research and Forecasting model (WRF-Chem) coupled with the SBM (Gao et al., 2016) was

127   employed to predict aerosol properties and their interactions with clouds and radiation for the AR

128   event on 6 - 9 February 2015. We focused on exploring the effects of INPs from sea spray

129   aerosols, in competition with mineral dust INPs, on the orographic mixed-phase clouds and

130   precipitation at different stages of the AR event as thermodynamic conditions evolved with the

131   different AR stages.

2 Model configuration and experiment design

The WRF-Chem version 3.6 coupled with SBM as described in Gao et al. (2016) is employed for model simulations of this study, in which SBM is coupled with the Model for Simulating Aerosol Interactions and Chemistry (MOSAIC; Fast et al., 2006; Zaveri et al., 2008). The SBM scheme is a fast version in which ice crystal and snow (aggregates) are represented with a single size distribution (low-density ice) with a separation at 150 μm in radius, and graupel or hail is for high-density ice represented with an additional size distribution (Khain et al., 2009, 2010; Fan et al., 2012, 2017a). Here we choose the graupel version since hail is not one of the major cloud hydrometeors in the case we simulate. The fall speed power law relationships for ice/snow and graupel are depicted in Xue et al. (2017). The WRF-Chem-SBM model is particularly designed to improve simulations of aerosol effects on clouds for complicated aerosol compositions and heterogeneous spatial distribution of aerosols. It has been applied in several studies including warm stratocumulus clouds (Gao et al., 2016), thunderstorms (Fan et al. 2020; Zhang et al., 2020), and supercell storms (Lin et al., 2020). Here WRF-Chem-SBM is employed, different from our previous studies in Fan et al. (2014, 2017a) which used WRF-SBM with prescribed aerosols, in order to explicitly simulate various aerosol types including marine aerosols and dust particles.

The four-sector MOSAIC aerosol module is chosen for the simulations of aerosols and the CBMZ (Carbon Bond Mechanism version Z) is used for gas-phase chemistry. The MOSAIC module treats nine major aerosol species (sulfate, nitrate, chloride, ammonium, sodium, black carbon, primary organics, other inorganics (OIN), and water). OIN is used as a surrogate of dust and the production of dust is parameterized with the dust transport model DUSTRAN (Shaw et al., 2008). Sea salt aerosol (a combination of sodium and chloride), as a surrogate for all SSA, is

155   parameterized as a function of sea-surface wind speed (Gong et al., 1997b, a). The dry diameters

156   of the particles over the four bins have a range of 0.039–0.156, 0.156–0.624, 0.624–2.5, and 2.5–

157   10.0 μm, respectively. For the total aerosol, aerosol size distribution over each section is

158   represented with a 2-moment approach that predicts aerosol mass and number following a log-

159   normal distribution (Simmel and Wurzler, 2006). For each composition such as dust and sea salt,

160   only the mass mixing ratio in each section is predicted and outputted. The aerosol number

161   mixing ratio in each bin is only predicted for the total aerosol. Therefore, in this study, the dust

162   and sea salt number mixing ratios used for ice nucleation parameterizations were derived based

163   on their respective mass mixing ratios by assuming the same size and density of all particles over

164   each bin, that is,

165
$$N_{i,j} = \frac{m_j}{6\pi (D_j)^3 \rho_i}$$

166   where i denotes the aerosol composition (sea salt or dust here), j denotes the jth aerosol bin, m_j is

167   the total mass mixing ratio of the jth bin, ρ_i is the assumed density (i.e., 2.6 g cm^{-3} for dust and

168   2.2 g cm^{-3} for sea salt), and D_j is the geometric mean diameter of jth bin. The approach for

169   deriving the number mixing ratio for each aerosol component has been used in the literature (i.e.,

170   Zhao et al., 2013). We understand that the assumption that all particles have the same size over

171   each bin may introduce some uncertainty. However, the size distribution of each aerosol

172   component is unknown in the model and any assumption on the size distribution might introduce

173   uncertainty.

174
175   **2.1 Implementing immersion freezing parameterization for marine INPs**

176   In the original SBM model, the ice nucleation accounting for both deposition ice

177   nucleation and condensation-freezing is parameterized based on Meyers et al. (1992) and Bigg

178   (1953) is employed for immersion and homogeneous drop freezing. Neither of the ice nucleation

179   parameterizations is connected with aerosols. Bigg (1953) was formulated based on the

180   stochastic hypothesis where the freezing probability is assumed proportional to drop mass and

181   the freezing rate is as a function of temperature without involving INPs. Fan et al. (2014, 2017a)

182   implemented DeMott et al. (2015) as an immersion freezing parameterization to investigate the

183   effects of dust INPs on orographic mixed-phase clouds and precipitation during CalWater 2011.

184   We adapted this implementation to WRF-Chem-SBM for this study to connect ice nucleation

185   with dust particles. Developed based on both laboratory data and field measurements, DeMott et

186   al. (2015) is an empirical parameterization for immersion freezing of natural mineral dust

187   particles. INP concentrations are quantified as functions of temperature and the total number

188   concentration of particles larger than 0.5 μm diameter. In our implementation, the dust number

189   mixing ratio for each aerosol bin is derived from its mass as detailed in the section above. The

190   total dust number mixing ratio inputted to DeMott et al. (2015) is the integration over 0.5 -10

191   μm.

192   To connect ice nucleation with sea spray aerosols, we implemented McCluskey et al.

193   (2018a, thereafter MC2018), which was developed for quantifying ice nucleating activity by

194   marine organics over the North Atlantic Ocean, in SBM following a similar approach as the

195   implementation of DeMott et al. (2015). The nucleation site density in MC2018 is described as

196    $$n_s = exp(-0.545(T - 273.15) + 1.012)$$

197   where n_s is the nucleation site density (m^{-2}) and T is the temperature (K). With n_s determined by

198   MC2018, the nucleated ice particle concentration is obtained following Niemand et al. (2012) as

199    $$\sum_{j=1}^{n} N_j = \sum_{j=1}^{n} N_{\text{tot},j}\{1 - \exp[-S_{\text{ae},j} n_s(T)]\}$$

200   where $S_{ae,j}$ is the surface area of individual sea spray aerosol particles in the jth bin which is

201   calculated from $\pi D_j^2/4$ (D_j is the geometric-mean diameter), $N_{tot,j}$ is the total sea spray aerosol

202   number in each bin which is derived from its mass as detailed in the section above, and N_j is the

203   ice particle number in each bin. Sea salt particles are used as the surrogate of sea spray aerosols

204   given that most marine organic aerosols exist with coating on the surface of sea salt particles in

205   the size range that dominates surface area (e.g., Prather et al., 2013).

206   Bigg et al. (1953) is employed only for homogeneous drop freezing when the temperature

207   is colder than -37 $^{\circ}$C. As discussed in Fan et al. (2014), the deposition-condensation freezing is

208   turned off because the simulation with deposition-condensation freezing produces a large

209   number of small ice particles, which is not consistent with the observed mixed-phase cloud

210   properties in the study region. Contact freezing is also turned off due to negligible contributions

211   (Fan et al., 2014).

212   **2.2 Experiment design**

213   Simulations are configured with two nested domains using the nesting down approach

214   (i.e., the inner domain is run separately driven by the outer domain), covering most of the

215   western US (Fig. 1). The outer domain consists of 399 × 399 grid points with a horizontal grid

216   spacing of 3 km and the inner domain consists of 498 × 390 grid points with a horizontal grid

217   spacing of 1 km. 50 vertical levels with stretched intervals are configured, with a grid spacing of

218   70 m at the lowest levels and ~400 m at the model top. The dynamics time step is 15 seconds for

219   the outer domain and 5 seconds for the inner domain.

220   The simulation for the outer domain starts at 00:00 UTC on February 3 and runs for 48

221   hours for chemistry spin-up using the WRF-Chem-SBM model, driven by global WRF-Chem

222   simulation as the initial and boundary conditions of gas-phase species and aerosols and the

223   Modern-Era Retrospective analysis for Research and Applications, Version 2 (MERRA2; spatial

224   resolution of 0.5 by 0.5 degree and temporal resolution of 6-hourly) as the initial and boundary

225   conditions of meteorological fields. Then the outer domain simulation is reinitialized at 00:00 UTC

226   on February 5 using the meteorological data from MERRA2 to avoid the large error growth in

227   meteorology associated with long-time model integration, although the chemistry simulation is a

228   continuation from the spin-up run and runs until 23:00 UTC on February 8. Given that running the

229   WRF-Chem-SBM fully-coupled model is extremely computationally expensive for 1-km grid

230   spacing in the inner domain, we interpolate aerosol-related quantities such as aerosol composition,

231   hygroscopicity, and mass and number concentrations from the outer domain simulations using

232   bilinear interpolation for the inner-domain simulation to reduce computational cost. This means

233   that we conduct the inner-domain simulation separately with chemistry turned off, and aerosol

234   information is updated hourly using data from the outer domain simulations. The inner-domain

235   simulation is run from 00:00 UTC on February 5 to 23:00 UTC on February 8, and the initial and

236   boundary meteorological conditions are from MERRA2. To validate this approach, we compared

237   the simulation with fully coupled WRF-Chem-SBM for the inner domain simulation and found

238   that the two simulations resemble each other in terms of precipitation (Fig. S1). Therefore, it is a

239   valid approach that saves computation time by about 40%.

240   For emissions data, the U. S. Environment Protection Agency (EPA) National Emission

241   Inventory (NEI) with a 4 km by 4 km horizontal resolution based on the year 2011 rates

242   (NEI2011) is commonly used for anthropogenic emissions in the United States. However, using

243   NEI2011 predicts too large anthropogenic aerosol mass compared with observations. Since the

244   emissions of gaseous species and particulate matter decreased significantly from 2011 to 2015 in

245   California (Table S1), the California Air Resources Board emission inventory in 2015

246 (CARB2015) is used for anthropogenic emissions input for California, while NEI2011 is used

247 for other states in the simulation domain. The use of NEI2011 for other states is acceptable since

248 the lower and middle atmosphere in the simulation domain is dominated by southwesterly winds

249 during the simulation period that transport air pollutants from coastal to inland regions. The use

250 of CARB2015 reduces the simulation of aerosol number concentrations mainly below 2 km. The

251 aerosol concentration averaged over 1-2 km altitudes is about 160 cm^{-3} with CARB2015 and 317

252 cm^{-3} with NEI2015, which is 26% lower and 47% higher than aircraft observations (215 cm^{-3}),

253 respectively. Thus, the simulated aerosol concentrations with CARB2015 are in better agreement

254 with observations.

255   The Model of Emissions of Gases and Aerosols from Nature (MEGAN) with a monthly

256 temporal and 1 km horizontal resolution (Guenther et al., 2012) is used for biogenic emissions.

257 The Rapid Radiative Transfer Model for application to GCMs (RRTMG) is used for shortwave

258 and longwave radiation schemes (Iacono et al., 2008), the Noah Land Surface Model for land

259 surface physics (Chen and Dudhia, 2001), and the Mellor-Yamada-Janjic (MYJ) scheme for

260 planetary boundary layer parameterization (Mellor and Yamada, 1982; Janjić and Prediction,

261 2001). Cumulus parameterization is not considered for the simulations over both domains.

262   Three simulations were carried out over the inner domain for this study to investigate the

263 impacts of marine INPs: (1) The reference case is Bigg, using the default immersion freezing

264 parameterization of Bigg et al. (1953) in SBM which is temperature-dependent only; (2)

265 DM15+MC18, in which both DeMott et al. (2015) and MC2018 parameterizations are used for

266 ice nucleation from dust and marine aerosols, respectively; (3) DM15, using the parameterization

267 of DeMott et al. (2015) for dust aerosols (diameter > 0.5 μm) with MC2018 turned off. The

268 impacts of marine INPs are derived by comparing the DM15+MC18 and DM15 simulations.

269

3 Case description and measurements

270 **3 Case description and measurements**

271   As introduced earlier, our study case is the AR event occurring during 5 - 9 February

272 2015 during the ACAPEX campaign and made landfall on the coast of Northern California,

273 producing heavy rainfall. Marine aerosols were the main aerosol type. Dust and biological

274 particles were rather scarce in and around the AR (Levin et al., 2019).

275   The AR evolution has three distinct stages: before AR landfall (from 06:00 UTC 5 to

276 18:00 UTC 6 February), after AR landfall (from 18:00 UTC 6 to 12:00 UTC 7 February), and

277 post-AR (from 12:00 UTC 7 to 09:00 UTC 8 February). The three stages can be identified from

278 the change of the integrated water vapor (IWV) with time during the event (Fig. 2a). Before AR

279 landfall, IWV in most of California was relatively low (Fig. 2a, left). The IWV in northern

280 California increased as the AR made landfall at about 18:00 UTC on 6 February and brought

281 ample water vapor to California (Fig. 2a, middle). Heavy orographic precipitation along the

282 Sierra Nevada Mountains occurred during this period. At 12:00 UTC 7 February, the AR started

283 to retreat (Fig. 2a, right), and postfrontal cloud cells formed, with relatively small cloud fraction

284 and precipitation.

285   Vertical profiles of the thermodynamic and kinematic environments at the three stages

286 are shown in Figs. 2b-d. The thermodynamic and kinematic environments significantly varied

287 with the AR stages. After AR landfall, water vapor increased significantly in the lower

288 atmosphere (below 5 km), but the middle and upper levels became drier (dashed, Fig. 2b)

289 compared with the stage before AR landfall (solid). The vertical motion also weakened after AR

290 landfall (Fig. 2d), suggesting that the atmosphere became more stable. At the post-AR stage,

291 moisture above 2-km altitude was reduced compared to after AR landfall. Note that the

292   temperature below 8 km was colder by up to 6 °C at the post-AR stage compared to the previous

293   two stages (Fig. 2c). These differences in the meteorological conditions among the different

294   stages are very important to understand the cloud and precipitation properties and their responses

295   to marine INPs.

296   Extensive in-situ and remote-sensing measurements are used to understand aerosol and

297   cloud properties and evaluate model results. The G-1 aircraft sampled the postfrontal clouds on

298   February 7 during 20:20-20:30 UTC.

299   Aerosol instruments on board the G-1 aircraft included (1) a Droplet Measurement

300   Technologies (DMT) ultrahigh sensitivity aerosol spectrometer (UHSAS), measuring dry fine

301   mode aerosol size spectra of 55–800 nm with sizing uncertainty of 2.5% (Uin, 2016); (2) a

302   Passive Cavity Aerosol Spectrometer Probe (PCASP) for coarse model aerosol spectra (0.1-3

303   μm) with +/-20% uncertainty in size and +/-16% in concentration (Goldberger, 2020), and (3)

304   Aerosol Time of Flight Mass Spectrometry (ATOFMS) measurements provided the mean

305   fractional number contributions of aerosol source classifications (Levin et al., 2019). Cloud

306   instruments include an FCDP (1.5-50 μm) with ~3 μm uncertainty in size (Glienke and Mei,

307   2020), and the two-dimensional stereo (2DS) probe with +/-10 μm size uncertainty to provide

308   cloud particle size spectra (Glienke and Mei, 2019). Uncertainty in the number concentration for

309   both probes follows Poisson's counting statistics. The LWC and IWC are derived from the Water

310   Content Monitor (WCM) on board the G-1 aircraft, an instrument that uses the impact of water

311   on several heated wires as the basis for measuring cloud total water content (TWC) and liquid

312   water content (LWC) from which the ice water content (IWC) can be derived (Baumgardner et

313   al., 2011; Matthews et al., 2015). Wind tunnel measurements indicate that ice contributes <1% to

314   the LWC elements response.

315   The Next Generation Radar (NEXRAD) radar reflectivity measurements were processed

316   and used for model evaluation. The original NEXRAD Level 2 data (polar coordinate) were

317   downloaded from AWS-NOAA NEXRAD S3 data service (https://registry.opendata.aws/noaa-

318   nexrad/). We mapped the data to a Cartesian coordinate with 2 km horizontal resolution and

319   approximately 5 min frequency using the Python ARM Radar Toolkit (Py-ART; Helmus and

320   Colis, 2016). The operational NEXRAD radar reflectivity uncertainties are 2 - 3 dB (Gourley et

321   al., 2003) and theoretical demonstrations with differing raindrop shape models yield radar

322   reflectivity biases of 1.2 dB (Gourley et al., 2009). The observed precipitation rates are from the

323   rain gauge measurements, provided by the NOAA Earth System Research Laboratory's Physical

324   Sciences Division (https://psl.noaa.gov/data/obs/datadisplay).

325   **4 Results**

326   **4.1 Model evaluation with observations**

327   We evaluate the model simulations of aerosol and cloud properties and surface

328   precipitation. Figure 3a shows a comparison of modeled aerosol properties including aerosol

329   number concentration and chemical composition from the simulation of DM15+MC18 intended

330   to represent the observed case, with the G-1 aircraft measurements on 7 February. Aerosol

331   properties in all three simulations are similar, and thus only DM15+MC18 is shown. Overall, the

332   simulated aerosol number concentration over the size range of 0.067 - 3 μm is comparable to the

333   observations over the same size range estimated by combining data from UHSAS and PCASP at

334   below 2-km altitude. The simulation overestimates the total aerosol number concentrations by ~

335   2-times averaged over the altitudes of 2.2-3.2 km. At 2.8 km, the difference between the

336   simulation (219 cm^{-3}) and observations (55 cm^{-3}) is about 4 times. The mean fractional number

337   contributions of aerosol composition classifications measured from ATOFMS are shown in Fig.

338 3b. For comparison with the model, the mean mass contributions of the corresponding aerosol

339 source classifications are computed since the number concentrations of individual aerosol

340 components are not predicted by WRF-Chem (Fig. 3c). Both the observed fractional number

341 contributions and the simulated mass contributions show that marine aerosols are dominant

342 during the AR event, accounting for more than 60% of the total aerosol number based on

343 ATOFMS measurements and total aerosol mass based on the simulation. Although the simulated

344 dust mass fraction is ~14%, the derived number concentration for sizes larger than 0.5 μm is very

345 low (less than 0.02 cm^{-3}, shown in a later figure). This is because the dust number concentration

346 is dominated by small particles (14.71 cm^{-3} for the sizes smaller than 0.5 μm). The number

347 concentrations of the sea salt aerosols are generally three orders of magnitude higher than those

348 of dust, and these numbers populate smaller bins of the aerosol distribution (97% from the first

349 two aerosol size bins) even though the sea salt mass is predominately at larger sizes (96% from

350 the last two size bins).

351   Figure 4 presents an evaluation of precipitation, showing the accumulated precipitation

352 during the AR event from 06:00 UTC 5 February to 09:00 UTC 8 February 2015 (Fig. 4a-b) and

353 the time-series of mean precipitation rates averaged over the observation stations (Fig. 4c-d). The

354 model generally captures the spatial pattern of the observed accumulated precipitation (Fig. 4a)

355 and reproduces the temporal evolution of precipitation (Fig. 4b). Two major precipitation periods

356 in the observations, including AR-induced orographic precipitation and postfrontal precipitation,

357 are generally captured in the simulations, although the simulated postfrontal precipitation occurs

358 several hours later in the simulations compared to the observations. All three simulations predict

359 a narrower but higher peak precipitation compared with the observed wider peak with lower

360 values (Fig. 4c). However, the overestimation of the peak value by DM15+MC18 is lower than

361   the other two (30% vs. 45% for DM15 and 58% for Bigg; Fig. 4c-d). The accumulated

362   precipitation in the southern mountain range (the southern part of white boxes in Fig. 4a) is

363   generally less than 100 mm in observations and less than 120 mm in DM15+MC18 but more

364   than 140 mm in the other two simulations. The mean precipitation over the white box

365   accumulated over the AR period are 89, 128, 130, and 116 mm for observations, Bigg, DM15,

366   and DM15+MC18, respectively. Again, although all three simulations overestimate the

367   precipitation, DM15+MC18 simulates the lowest value and is closer to observations.

368   DM15+MC18 predicts more precipitation (i.e., 48 mm for the mean accumulated precipitation)

369   than the other two simulations (i.e., 45 mm in Bigg and 42 mm in DM15). The simulated

370   precipitation between Bigg and DM15 is very similar except for more precipitation in Bigg in the

371   northern part of the domain (Fig. 4a-b), suggesting that in a low dust environment, the

372   temperature-dependent Bigg (1953) parameterization simulates similar ice formation as DeMott

373   et al. (2015). There is a clear spillover effect caused by marine INPs (Fig. 4a-b, right). That is,

374   with marine INPs considered in DM15+MC18, there is a notable decrease in accumulated

375   precipitation (~ 30-50 mm) on the windward side but a large increase (~ 50-70 cm) on the lee

376   side (Fig. 4b, right). This is because more ice/snow formed over the windward side falls slower

377   than rain and more of them are transported to the lee side, which will be discussed more in

378   section 4.2.

379   Cloud phase is crucial to radiation and precipitation for mixed-phase clouds, and the

380   glaciation ratio is usually used to represent the cloud phase states. The glaciation ratio is defined

381   as IWC/(IWC+LWC), where LWC and IWC denote liquid and ice water content, respectively.

382   Values less than 0.1 and larger than 0.9 denote the liquid phase and ice phase, respectively, with

383   values between 0.1 and 0.9 for the mixed-phase (Korolev et al., 2003). The G-1 aircraft sampled

384   the postfrontal clouds on February 7 as shown in Fig. 5a. All three simulations cannot capture the

385   observed size of the precipitation cell (Figs. 5b and S2). In the simulations, precipitation is

386   dominated by a few heavy precipitation clusters instead of the observed wide precipitation area.

387   The simulated cells also do not reach the high altitudes found in the observations. The deviations

388   of the simulation from observations for the postfrontal clouds could be because of various

389   reasons such as (a) the long-time model integration time (the 4th day after model initiation) and

390   (b) the spatial mismatch of simulated and observed clouds since those postfrontal clouds are

391   small. Anyhow, DM15+MC18 simulates the largest size of the precipitation cell, with the

392   highest vertical extent among the three simulations.

393   LWC and IWC along both horizontal and vertical flight segments are displayed in Figs.

394   6a-b. IWC is generally 2-4 times larger than LWC in the postfrontal clouds. To compare with

395   observations, the model data are processed by: (a) selecting the grids at a distance from the

396   simulated cell center similar to the distance of the airplane position from the observed postfrontal

397   cell center, and sampling the data at a similar ambient temperature as observed by the aircraft

398   (around -10 $^{\circ}$C along the horizontal segment shown in Fig. 6a); (b) accounting for the location

399   mismatch and increasing the sample size in the simulation to be more representative by

400   extending the sampling area to include 20 grids at the front and back of a selected grid along the

401   flight track, mimicking approximately the distance traveled by the G-1 airplane in five minutes;

402   (c) filtering out the sampled grids with values of (LWC + IWC) below the detection limit of

403   WCM (i.e., 0.02 g m^{-3}, Thompson et al., 2016). Both horizontal and vertical flight segments are

404   incorporated for comparison.

405   Figure 6c and d shows comparisons of LWC, IWC, and the glaciation ratio of

406   IWC/(IWC+LWC) between the simulations and aircraft measurements. The LWC is

407   overestimated in all three simulations with DM15+MC18 of the largest overestimation (6 times

408   higher than observations), while IWC is underestimated in Bigg and DM15 (nearly an order of

409   magnitude lower in DM15 than observations) (Fig. 6c). DM15+MC18 predicts much higher

410   IWC than the other two simulations, with an overestimation of IWP by ~3 times. The mean

411   glaciation ratios fall in the range of 0.1- 0.9 among the simulations (Fig. 6d), indicating that the

412   observed mixed-phase cloud feature is simulated by the model. DM15+MC18 shows a mean

413   ratio of ~ 0.70, similar to the observed value of 0.74. This shows that the mixed-phase state is

414   well captured when the marine INP effect is considered. In contrast, in Bigg and DM15 with a

415   glaciation ratio of 0.41 or less, the mixed-phase state is liquid-dominated. The inclusion of the

416   marine INP effect improves the simulation of cloud phase states via enhancing heterogeneous ice

417   formation through immersion freezing. But the overestimated LWC and IWC at this post-AR

418   stage might have implications to marine INP effects. Here it is already indicated that the modeled

419   post-frontal clouds are very sensitive to marine INPs. A detailed examination of how the marine

420   INPs impact ice nucleation and cloud properties will be discussed in the following section.

421

422   **4.2 Marine INP effects under different AR stages**

423   Impacts of the marine INPs transported from the Pacific Ocean on orographic clouds and

424   precipitation are revealed by comparing the simulation of DM15+MC18 with the simulation of

425   DM15.

426   As described in Section 3 about the AR evolution, before AR landfall (from 06:00 UTC 5

427   to 18:00 UTC 6 February), precipitation occurred in northern California. After AR landfall (from

428   18:00 UTC 6 to 12:00 UTC 7 February), heavy orographic precipitation along the Sierra Nevada

429   Mountains occurred (Fig. 7a). At the post-AR stage (from 12:00 UTC 7 to 09:00 UTC 8

430   February), scattered postfrontal cloud cells formed, with relatively small cloud fractions and

431   precipitation (Fig. 7a). The mean water vapor and temperature profiles are very different

432   between different AR stages, but the two simulations – DM15 (blue) and DM15+MC18 (red) –

433   predict very similar results as seen from the overlapping blue and red lines.

434   From the time series of average precipitation rates (Fig. 7a), the effect of marine INPs

435   varies with the different AR stages, from the large increases of precipitation (over 50% in

436   general) before AR landfall (the red dotted line, second y-axis) to no significant effects (a very

437   small increase) after AR landfall. In the first stage (before AR landfall), the total precipitation

438   increases by 36% on average due to the marine INP effect (Fig. 7a and Table 1). There is only a

439   4% increase in the total precipitation after AR landfall. Note that precipitation is small at some

440   point before AR landfall, so the large increases might not mean that much. The total precipitation

441   at the post-AR stage is negligible and the change in domain-mean precipitation from DM15 and

442   DM15+MC18 is also small. Thus, the marine INP effect only significantly increases the total

443   precipitation over the domain at the stage before AR landfall when a moderate amount of

444   precipitation occurs in northern California (Fig. 8a). After AR landfall, precipitation increases

445   significantly. Although the total precipitation is not changed much by the marine INPs, the

446   marine INPs produce a spillover effect featuring reduced precipitation on the windward slope of

447   the mountains but increase precipitation over the lee side (Fig. 8b and Fig. 9e). This is because

448   with the marine INPs, the larger amount of ice/snow that forms on the windward slope is

449   transported to the lee side (Fig. 9d) and grows to a larger size and precipitates as snow. This

450   spillover effect is accompanied by a large reduction of cloud water and rain over the windward

451   side because of the conversion of liquid to ice (Fig. 9b-c). Since the water vapor transport along

452   the cross-section is very similar between DM15 and DM15+MC18 (Fig. 9a), the spillover effect

453   by marine INPs is mainly the result of different cloud microphysical properties instead of

454   meteorological conditions.

455   Even though the total domain precipitation is not changed much by the marine INPs at

456   the latter two stages, the cloud phase and the near-surface precipitation type (i.e., rain or snow)

457   are notably changed (Table 1). The mean glaciation ratio in the mixed-phase is very low in

458   DM15 (0.14, 0.16, and 0.001 for the 1st, 2nd, and 3rd stages, respectively) and is increased in

459   DM15+MC18 to 0.74, 0.59, and 0.36, respectively. We examine the ratio of snow/(rain+snow)

460   in mass mixing ratio at the lowest model level for the changes of the near-surface precipitation

461   type (Fig. 7b). There is negligible snow precipitation near the surface in DM15 and the ratios of

462   snow precipitation are very small during the entire AR event. The snow precipitation ratios

463   increase in DM15+MC18 and the magnitudes vary significantly with different AR stages. On

464   average, the ratio of snow precipitation increases from 0.002, 0.001, <0.001 in DM15 to 0.08,

465   0.04, and 0.13 in DM15+MC18 before AR landfall, after AR landfall, and post-AR, respectively

466   (Table 1). This shows that marine INPs increase snow precipitation and the effect is particularly

467   significant before AR landfall and post-AR. Correspondingly, rain precipitation is reduced

468   (Table 1). This has an important implication for the regional hydrological resource since more

469   snow accumulation in winter increases freshwater resources in the summer while less rain

470   reduces flood risks.

471   The increased snow and reduced rain at the surface correspond to the increased ice water

472   path (IWP) and decreased liquid water path (LWP; Fig. 7c). The mean LWP in DM15+MC18 is

473   reduced by 66%, 46%, and 26% for the three stages relative to DM15, respectively (Table 1). We

474   showed an increased LWC from DM15 to DM15+MC18 in Fig. 6c in the postfrontal cells. Here

475   the decrease in LWC/LWP averaged over the entire post-AR stage is dominated by the strong

476 decrease over the time before the postfrontal cloud formed. Both LWC and IWC are increased by

477 marine INPs as shown in Fig. 6 (see section 4.3 for more discussion). IWP is greatly enhanced

478 by about 8, 5, and 440 times at the three stages, respectively. Interestingly, the total condensate

479 water path (TWP) is increased by the marine INPs (Fig. 7d). On average there are 45%, 29%,

480 and 35% increases in TWP in DM15+MC18 at the three AR stages relative to DM15,

481 respectively (Table 1). The increases in the total condensate water path and the increased surface

482 precipitation (or no change) suggest that marine INPs enhance the conversion of water from the

483 vapor phase to the condensate phase, which will be further discussed later. This is particularly

484 the case before AR landfall, with water vapor content notably reduced in DM15+MC18

485 compared with DM15 (Fig. S3a).

486 Cloud cover is slightly increased during the first two stages (4-5%) in the simulations

487 considering marine INPs, but the change at the post-AR stage is ~ 20% on average, which is very

488 significant. Because both TWP and cloud cover are increased due to the marine INP effect, the

489 cloud radiative forcing (CRF) at TOA gets stronger by 15%, 13%, and 10% for the three AR

490 stages, respectively. Although the cloud phase, precipitation type, and cloud fraction at the post-

491 AR stage have the largest changes among the three stages by the marine INP effect (Table 1), the

492 CRF does not change drastically probably because of the offset between the increase resulting

493 from the increased cloud fraction and TWP and the decrease from the reduced cloud liquid is the

494 largest.

495 Overall, the marine INP effects on TWP, IWP, and snow precipitation are more

496 significant at the first and third stages (i.e., before AR landfall and post-AR) than the stage after

497 AR landfall, but a notable spillover effect is seen after AR made landfall. Cloud and

498 precipitation quantities are more sensitive to marine INPs before AR landfall than after AR

499   landfall, and the responses of TWP/IWP and snow precipitation are particularly drastic at the

500   post-AR stage (Table 1). As noted earlier, we should not put much attention on the marine INP

501   effects at the post-AR stage since our model seems not be able to capture those small cloud cells

502   well. The reasons leading to the different responses at different AR stages are now examined.

503   **4.3 Explaining different marine INP effects at different AR stages**

504   We first examine the temporal evolution of dust and marine aerosol number

505   concentrations, which are derived based on the predicted mass mixing ratios as described in

506   Section 2 and used as input to the DeMott et al. (2015) and MC2018 parameterizations (Fig. 10a,

507   b), as well as their corresponding immersion freezing (i.e., ice nucleation) rates (Fig. 10c, d). The

508   dust concentrations and the corresponding ice nucleation rates (Fig. 10a, c) are about three orders

509   of magnitude lower than those of the marine aerosols (Fig. 10b, d) during the AR events. Ice

510   nucleation from dust is negligible at temperatures warmer than -15 ºC but the ice nucleation from

511   marine aerosols is notable. This is mainly because of three orders of magnitude higher marine

512   aerosol number concentrations from the surface up to 8 km since ice nucleation efficiencies of

513   marine aerosols are about three orders of magnitude lower than mineral dust at any temperature

514   (MC2018). The deep marine aerosol layer during the AR allows notable ice nucleation at

515   temperatures even higher than -15 ºC. Homogenous freezing (< -37 ºC; Fig. 10d vs. 10c) occurs

516   less in DM15+MC18 because of a larger consumption of liquid drops and supersaturation in the

517   heterogeneous freezing regime. This is commonly seen in convective clouds (e.g., Zhao et al.

518   2019). The clear-sky marine aerosol number concentrations increase from before AR landfall to

519   post-AR as the AR evolved (Fig. 10b). After the AR made landfall, marine aerosols increase

520   significantly as AR strong winds near the ocean surface produce more of them and also transport

521   more to the Sierra Nevada Mountains (Fig. 10b). Despite the significant increase in marine

522   aerosols after AR landfall, the marine INP effects on clouds and precipitation are small at this

523   stage, because the increase of marine aerosols does not increase ice nucleation rates (Fig. 10d).

524   However, at the post-AR stage, the ice nucleation rates from the marine INPs are up to a few

525   times larger than the earlier two stages (Fig. 10d), explaining why the effects on IWP and snow

526   precipitation at the post-AR stage are largest among the three stages.

527   To further understand how and why cloud and precipitation responses to marine INPs are

528   different at different AR stages, we separate clouds into three cloud regimes: a shallow warm

529   cloud regime with cloud top temperature (CTT) warmer than 0 °C, a mixed-phase cloud regime

530   with CTT between -30 and 0 °C, and a deep cloud regime having CTT colder than -30 °C and

531   cloud base temperatures above 0 °C. Figure 11 shows that the marine INP effect consistently

532   shifts the cloud occurrences from the shallow warm cloud regime to mixed-phase and/or deep

533   cloud regimes among the three AR stages. It is noted that the deep cloud regime is enhanced

534   much more at the first and third stages than the second stage, i.e., 22% before AR landfall and

535   235% at the post-AR stage but only 8% after AR landfall. The post-AR stage also has the largest

536   increase in mixed-phase cloud occurrences.

537   Accordingly, the mean cloud depth for each cloud regime is changed by marine INPs,

538   with a decrease for the shallow warm clouds and an increase for the mixed-phase and deep

539   clouds (Fig. 11b). Before AR landfall, the increase in the deep cloud depth is largest while at the

540   post-AR stage, the increase in the mixed-phase cloud depth is the largest. Consistent with a shift

541   in cloud regimes, the total precipitation produced by shallow warm clouds is reduced by 9%,

542   22%, and 16% while the total precipitation produced by deep clouds is increased by 66%, 4%,

543   and 350%, respectively, at the three AR stages (Fig. 11c). Therefore, the large increase in the

544   surface accumulated precipitation by marine INPs before AR landfall (36%) is mainly because of

545   the increase in deep cloud precipitation. The larger occurrence of deep clouds at this stage is

546   consistent with a larger increase in TWP and reduction in moisture. Although the relative

547   increases in deep cloud occurrences and precipitation by marine INPs are very large at the post-

548   AR stage, their occurrences are so small that their contribution to the total precipitation is

549   negligible. The effects of marine INPs on the postfrontal clouds might differ from the reality

550   since based on very limited measurement data, the model seems not be able to capture those

551   clouds well. The overestimated supercooled LWC can allow for more riming growth which may

552   lead to a larger sensitivity to marine INPs.

553   How do marine INPs reduce shallow warm clouds but increase mixed-phase and deep

554   clouds and why is this effect larger at the first and third stages? Marine INPs greatly enhance ice

555   and snow number concentrations and mass mixing ratios through immersion freezing, which

556   converts drops to ice or snow particles (Figs. 12a and 13a). The mean number concentrations

557   and mass mixing ratios of ice particles (ice +snow) in mixed-phase and deep cloud regimes are

558   several orders of magnitude higher in DM15+MC18 than in DM15. As detailed in Fan et al.

559   (2017a) which studied the same type of mixed-phase clouds in the same region, more ice/snow

560   particles forming from the immersion freezing enhance the Wegener–Bergeron–Findeisen

561   (WBF) and riming processes (Table 2), converting supercooled drops to ice or snow and leading

562   to more ice/snow but fewer cloud droplets and raindrops (Figs. 12b, c and 13b, c). The

563   reductions of cloud droplet and raindrop number concentrations and mass mixing ratios from

564   DM15 to DM15+MC18 are larger before AR landfall and during post-AR relative to the stage

565   after AR landfall, corresponding to a larger shift to the mixed-phase and deep clouds. Thus, the

566   larger increases in deposition/WBF and riming rates are seen (Table 2).

567   As discussed earlier, the largest ice nucleation rates from marine aerosols at the post-AR

568   stage explain the largest marine INP effects among the three stages. The factors contributing to

569   the larger ice nucleation rates include the increased abundance of marine aerosols compared to

570   the previous two stages (Fig. 10b). In addition, with the ~ 6 ºC colder temperatures below 8-km

571   altitudes during the post-AR stage compared to the other two stages, ice nucleation from marine

572   aerosols becomes more efficient (Fig. 10d). The increase in both LWC and IWC and a large

573   increase in cloud fraction for postfrontal cloud cells by the marine INP effect might also be

574   related to small scale thermodynamic changes through the feedback of microphysical changes

575   over the first two AR stages.

576   As for why increases of deep cloud occurrence and precipitation are less significant after

577   AR landfall compared to before AR landfall, first, the moisture increase after AR landfall occurs

578   in the lower atmosphere while the middle- and upper-level atmosphere are much drier than

579   before AR landfall (Fig. 2d), which favors more warm clouds and rain but is less favorable to ice

580   cloud development as indicated by the smallest ratio of snow precipitation (Fig. 7b). For more

581   warm clouds/rain-dominated situations, the enhancement of ice formation would have less

582   influence. Furthermore, in the drier conditions aloft, more ice formation means less efficient

583   growth, thus the impacts on IWC/IWP and precipitation would be smaller. Cloud dynamics

584   (vertical velocity) is not changed much by the marine INP effect at all three stages, indicating

585   that the feedback from the increased latent heating resulting from enhanced deposition and

586   riming does not play an important role here, likely because this is not a convective environment.

587   **5 Conclusion and discussion**

588   We have explored the effects of INPs from sea spray aerosols transported from the

589   Pacific Ocean on wintertime mixed-phase stratiform cloud properties and precipitation

590   associated with atmospheric river (AR) events. This is done by carrying out simulations at a

591   cloud-resolving scale (1 km) using WRF-Chem coupled with the spectral-bin microphysics

592   (SBM) scheme for an AR event observed during the 2015 Atmospheric Radiation Measurement

593   Cloud Aerosol Precipitation Experiment (ACAPEX). We have implemented ice nucleation

594   parameterization for sea spray aerosols (McCluskey et al. 2018a) into SBM to account for the

595   marine INP effect. By comparing with ground-based observations, we show that considering the

596   marine INP effect in the model improves the simulation of AR-precipitation. Based on the

597   evaluation with limited data from aircraft measurements, it appears the marine INP effect

598   improves the cloud phase states (i.e., increased glaciation ratio) in the post-AR but overestimates

599   condensate mass.

600   Through enhancing ice and snow formation, marine INPs greatly enhance WBF and

601   riming processes, which convert liquid clouds to mixed-phase and ice clouds. There is a notable

602   shift in cloud occurrences with reduced shallow warm clouds (44%, 26%, and 7% for before and

603   after AR landfall and the post-AR stages, respectively) and increased mixed-phase (10%, 7%,

604   and 38%) and/or deep cloud regimes (~ 22%, 8%, and 230%) because of the marine INP effect.

605   As a result, large increases in the ice water path (5 times or more), total condensate water path

606   (29% or more), and the ratio of snow precipitation (40 times or more) are seen. There is an

607   enhanced conversion of water from the vapor phase to the condensate phase so the water vapor is

608   generally reduced with the marine INP effect considered.

609   The significance of the above-described marine INP effects varies with the AR stages,

610   with a larger effect before AR landfall and post-AR than after AR landfall that has the dominant

611   precipitation. Note that the marine INP effects on cloud properties and snow precipitation are

612   still notable even at the stage after AR landfall. Although the total precipitation is not much

613 changed, the drastic increase of snow precipitation and reduced rain precipitation at the surface

614 have an important implication for the regional water resources and flood risks since more snow

615 increases freshwater resources while less rain reduces flash flood risks. In addition, at this stage,

616 the marine INPs produce a notable spillover effect with a precipitation decrease (up to 30%) over

617 the windward slope of the mountains but precipitation (snow) over the lee side is doubled,

618 because more ice/snow formed over the windward side falls slower than rain and is more easily

619 transported to the lee side.

620  Several factors can be responsible for the smaller marine INP effects on cloud properties

621 (particularly reduction of shallow warm clouds and increased mixed-phase and deep clouds) and

622 snow precipitation after AR landfall compared with before AR landfall. First, after AR landfall,

623 the moisture is heavily concentrated at the lower atmosphere while the middle- and upper-level

624 atmosphere is much drier than before AR landfall. Therefore, the environment is more warm

625 cloud and rain dominated, limiting the effects of enhanced ice formation. Furthermore, in drier

626 conditions, more ice formation means less efficient growth, thus the impacts on IWC/IWP and

627 precipitation would be smaller.

628  The post AR stage has the largest response of the cloud regime shift and snow

629 precipitation among the three stages, because of the largest ice nucleation rates from the marine

630 aerosols. The larger ice nucleation rates compared with the other two stages are probably

631 because the abundance of marine aerosols is increased and also with ~ 6 °C colder temperatures

632 below 8-km altitudes than the other two stages, ice nucleation from the deep marine aerosol layer

633 is more efficient. Since our model may not simulate clouds well at the post AR stage based on

634 very limited measurement data, we emphasize that the large responses to marine INPs simulated

635 at this stage might not reflect the effect in reality.

636 This study suggests that the inclusion of marine INPs enhances orographic precipitation

637 mainly through more efficient growth (deposition and riming) of a larger number of ice particles

638 than liquid droplets, which is consistent with literature studies (Mühlbauer and Lohmann, 2009;

639 Fan et al., 2014, 2017; Xiao et al., 2015). The spillover effect by the increase of CCN has been

640 presented in several previous studies (e.g., Mühlbauer and Lohmann, 2008, 2009; Saleeby et al.,

641 2011, 2013; Carrio and Cotton, 2014; Letcher and Cotton, 2014). To our knowledge, this study is

642 the first to show the spillover effect associated with the INP effect. The prominent spillover

643 effect by the marine INP is different from Fan et al. (2014, 2017) that did not find such an effect

644 by dust INPs. There are a couple of factors that might be responsible for the difference. First,

645 marine INPs are mainly brought by ARs so the windward side gets INP first while dust INPs are

646 not associated with AR so there is no temporal sequence to have dust between the windward and

647 Lee sides. Second, the AR event is different with a different wind direction and speed, which

648 makes the transport of ice/snow to the lee side easier in this case.

649 The marine INP effect revealed in this study is clearly manifested due to the very low

650 dust INP concentrations for this particular situation and the high abundance of marine aerosols

651 during the AR which allows notable ice nucleation even at temperatures higher than -15 ºC. This

652 higher abundance of marine aerosols overcomes the fundamental lower efficiency of marine

653 INPs compared to dust INPs. With high dust INPs, the effects of marine INPs might not be as

654 significant since they compete for supercooled liquid drops. Although this is a single case study,

655 the AR event and its evolution are representative. Thus, the study suggests the importance of

656 accounting for marine aerosols as INPs, in addition to long-range transported mineral dust, to

657 simulate winter clouds and precipitation in the western United States in regional and global

658 climate models. We employ an empirical parameterization for marine INPs developed from the

659 data collected over the northern Atlantic Ocean and use sea salt aerosols as a surrogate of sea

660 spray aerosols, which might produce some uncertainties. Nevertheless, the marine INP

661 parameterization appears representative of this region based on Levin et al. (2019). More

662 observational data particularly on the extended spatial and temporal coverage are needed in the

663 western U.S. for (a) evaluating model simulations more robustly, (b) developing ice nucleation

664 parameterizations for potentially variable marine organics and (c) understanding marine organics

665 emission and chemical mechanisms and accurately simulating marine organics in the model. As

666 discussed earlier, the conversion of mass to number concentrations over each aerosol bin might

667 introduce some uncertainty to this study, which calls for model developments of predicting the

668 number concentration of each aerosol component.

669

670 **Data availability.**

671 The observational data can be accessed from the ARM data archive,

672 https://www.arm.gov/research/campaigns/amf2015apex. The model simulation data will be

673 available through the NERSC data repository after the paper is accepted.

674

675 **Supplement.**

676 The supplement related to this article is available online at:

677

678 **Author contributions.**

679 JF designed the study and model experiments. YL, JF, and PL performed numerical simulations

680 and analyses. JF and YL wrote the paper and other authors commented on it. LRL, PJD, LG, JF,

681 JT, YL, and JHJ contributed by either processing data including model input and observational

682 data or participating in the discussion of results.

683

684 **Competing interests.**

685 The authors declare that they have no conflict of interest.

686 **Acknowledgments.**

687 This research used resources of the PNNL Institutional Computing (PIC), and National Energy

688 Research Scientific Computing Center (NERSC). NERSC is a U.S. DOE Office of Science User

689 Facility operated under Contract No. DE-AC02-05CH11231. Funding for ACAPEX that

690 provides data collected on the G-1 aircraft was supported by the Atmospheric Radiation

691 Measurement (ARM) user facility, a U.S. Department of Energy (DOE) Office of Science user

692 facility managed by the Office of Biological and Environmental Research. The deployment of

693 the G-1 also involved the assistance of many PNNL/ARM field staff including M. Hubbell and

694 C. Eveland who flew the G-1 during ACAPEX. The authors acknowledge California Air

695 Resources Board for providing the 2015 emission inventory data and Dr. Allen White from

696 NOAA's Physical Sciences Laboratory for providing rainfall gauge data, and thank Alyssa

697 Matthews and Jingyu Wang at PNNL and Yuan Wang at JPL for technical/data discussion.

698

699 **Financial support.**

700 This study was supported by the Office of Science of U.S. Department of Energy Biological and

701 Environmental Research through the Regional and Global Model Analysis program area that

702 supports the Water Cycle and Climate Extremes Modeling (WACCEM) Science Focus Area at

703 PNNL and the DOE Early Career Research Program (project # 70071). PNNL is operated for the

704   U.S. Department of Energy (DOE) by Battelle Memorial Institute under contract DE-AC05-

705   76RL01830.

Reference

Ault, A. P., Williams, C. R., White, A. B., Neiman, P. J., Creamean, J. M., Gaston, C. J., Ralph, F. M., and Prather, K. A.: Detection of Asian dust in California orographic precipitation, J. Geophys. Res.-Atmo., 116, 1–15, https://doi.org/10.1029/2010JD015351, 2011.

Baumgardner, D., Brenguier, J. L., Bucholtz, A., Coe, H., DeMott, P., Garrett, T. J., Gayet, J. F., Hermann, M., Heymsfield, A., Korolev, A., Kramer, M., Petzold, A., Strapp, W., Pilewskie, P., Taylor, J., Twohy, C., Wendisch, M., Bachalo, W., and Chuang, P.:Airborne instruments to measure atmospheric aerosol particles, clouds and radiation: A cook's tour of mature and emerging technology, Atmos. Res., 102(1), 10–29, 10.1016/j.atmosres.2011.06.021, 2011.

Bigg, E. K.: The Formation of Atmospheric Ice Crystals by the Freezing of Droplets, Q. J. Roy. Meteorol. Soc., 79, 510–519, https://doi.org/10.1002/qj.49707934207, 1953.

Burrows, S. M., Hoose, C., Pöschl, U., and Lawrence, M. G.: Ice nuclei in marine air: Biogenic particles or dust?, Atmos. Chem. Phys., 13, 245–267, https://doi.org/10.5194/acp-13-245-2013, 2013.

Carrió, G.G., Cotton, W.R., 2014. On the buffering of CCN impacts on wintertime orographic clouds: an idealized examination, Atmos. Res. 137, 136–144.

Chen, F. and Dudhia, J.: Coupling an Advanced Land Surface–Hydrology Model with the Penn State–NCAR MM5 Modeling System. Part I: Model Implementation and Sensitivity, Mon. Weather Rev., 129, 569–585, https://doi.org/https://doi.org/10.1175/1520-0493(2001)129<0569:Caalsh>2.0.Co;2, 2001.

Choularton, T. W. and Perry, S. J.: A model of the orographic enhancement of snowfall by the seeder-feeder mechanism, Q. J. Roy. Meteorol. Soc., 112, 335–345, https://doi.org/https://doi.org/10.1002/qj.49711247204, 1986.

Choudhury, G., B. Tyagi, J. Singh, C. Sarangi, S.N. Tripathi. Aerosol-orography-precipitation – a critical assessment, Atmos. Environ., 214 (116831) (2019), pp. 1-19, 10.1016/j.atmosenv.2019.116831.

Cordeira, J. M., Ralph, F. M., Martin, A., Gaggini, N., Spackman, J. R., Neiman, P. J., Rutz, J. J., and Pierce, R.: Forecasting atmospheric rivers during CalWater 2015, Bull Am. Meteorol. Soc., 98, 449–459, https://doi.org/10.1175/BAMS-D-15-00245.1, 2017.

Creamean, J. M., Suski, K. J., Rosenfeld, D., Cazorla, A., DeMott, P. J., Sullivan, R. C., White, A. B., Ralph, F. M., Minnis, P., Comstock, J. M., Tomlinson, J. M., and Prather, K. A.: Dust and Biological Aerosols from the Sahara and Asia Influence Precipitation in the Western U.S, Science, 339, 1572–1578, https://doi.org/10.1126/science.1227279, 2013.

Creamean, J. M., Ault, A. P., White, A. B., Neiman, P. J., Ralph, F. M., Minnis, P., and Prather, K. A.: Impact of interannual variations in sources of insoluble aerosol species on orographic precipitation over California's central Sierra Nevada, Atmos. Chem. Phys., 15, 6535–6548, https://doi.org/10.5194/acp-15-6535-2015, 2015.

DeMott, P. J., Prenni, A. J., Liu, X., Kreidenweis, S. M., Petters, M. D., Twohy, C. H., Richardson, M. S., Eidhammer, T., and Rogers, D. C.: Predicting global atmospheric ice nuclei distributions and their impacts on climate, Proc. Nat. Acad. Sci. U.S.A., 107, 11217–11222, https://doi.org/10.1073/pnas.0910818107, 2010.

DeMott, P. J., Prenni, A. J., McMeeking, G. R., Sullivan, R. C., Petters, M. D., Tobo, Y., Niemand, M., Möhler, O., Snider, J. R., Wang, Z., and Kreidenweis, S. M.: Integrating laboratory and field data to quantify the immersion freezing ice nucleation activity of

750   mineral dust particles, Atmos. Chem. Phys., 15, 393–409, https://doi.org/10.5194/acp-15-
751   393-2015, 2015.
752 DeMott, P. J., Hill, T. C. J., McCluskey, C. S., Prather, K. A., Collins, D. B., Sullivan, R. C.,
753   Ruppel, M. J., Mason, R. H., Irish, V. E., Lee, T., Hwang, C. Y., Rhee, T. S., Snider, J. R.,
754   McMeeking, G. R., Dhaniyala, S., Lewis, E. R., Wentzell, J. J. B., Abbatt, J., Lee, C.,
755   Sultana, C. M., Ault, A. P., Axson, J. L., Martinez, M. D., Venero, I., Santos-Figueroa, G.,
756   Stokes, M. D., Deane, G. B., Mayol-Bracero, O. L., Grassian, V. H., Bertram, T. H.,
757   Bertram, A. K., Moffett, B. F., and Franc, G. D.: Sea spray aerosol as a unique source of ice
758   nucleating particles, Proc. Nat. Acad. Sci. U.S.A., 113, 5797–5803,
759   https://doi.org/10.1073/pnas.1514034112, 2016.
760 Dettinger, M. D., Ralph, F. M., Das, T., Neiman, P. J., and Cayan, D. R.: Atmospheric Rivers,
761   Floods and the Water Resources of California, Water-Sup., 3(2), 445-478,
762   https://doi.org/10.3390/w3020445, 2011.
763 Fan, J., Leung, L. R., Li, Z., Morrison, H., Chen, H., Zhou, Y., Qian, Y., and Wang, Y.: Aerosol
764   impacts on clouds and precipitation in eastern China: Results from bin and bulk
765   microphysics, J. Geophys. Res., 117, https://doi.org/https://doi.org/10.1029/2011jd016537,
766   2012.
767 Fan, J., Leung, L. R., DeMott, P. J., Comstock, J. M., Singh, B., Rosenfeld, D., Tomlinson, J.
768   M., White, A., Prather, K. A., Minnis, P., Ayers, J. K., and Min, Q.: Aerosol impacts on
769   California winter clouds and precipitation during CalWater 2011: local pollution versus
770   long-range transported dust, Atmos. Chem. Phys., 14, 81–101, https://doi.org/10.5194/acp-
771   14-81-2014, 2014.
772 Fan, J., Han, B., Varble, A., Morrison, H., North, K., Kollias, P., Chen, B., Dong, X.,
773   Giangrande, S. E., Khain, A., Lin, Y., Mansell, E., Milbrandt, J. A., Stenz, R., Thompson,
774   G., and Wang, Y.: Cloud-resolving model intercomparison of an MC3E squall line case:
775   Part I—Convective updrafts, J. Geophys. Res.-Atmo., 122, 9351–9378,
776   https://doi.org/10.1002/2017JD026622, 2017a.
777 Fan, J., Leung, L. R., Rosenfeld, D., and DeMott, P. J.: Effects of cloud condensation nuclei and
778   ice nucleating particles on precipitation processes and supercooled liquid in mixed-phase
779   orographic clouds, Atmos. Chem. Phys., 17, 1017–1035, https://doi.org/10.5194/acp-17-
780   1017-2017, 2017b.
781 Fast, J. D., Gustafson Jr., W. I., Easter, R. C., Zaveri, R. A., Barnard, J. C., Chapman, E. G.,
782   Grell, G. A., and Peckham, S. E.: Evolution of ozone, particulates, and aerosol direct
783   radiative forcing in the vicinity of Houston using a fully coupled meteorology-chemistry-
784   aerosol model, J. Geophys. Res.-Atmo., 111,
785   https://doi.org/https://doi.org/10.1029/2005jd006721, 2006.
786 French, J. R., Friedrich, K., Tessendorf, S. A., Rauber, R. M., Geerts, B., Rasmussen, R. M.,
787   Xue, L., Kunkel, M. L., and Blestrud, D. R.: Precipitation formation from orographic cloud
788   seeding, Proc. Nat. Acad. Sci. U.S.A., 115, 1168 LP – 1173,
789   https://doi.org/10.1073/pnas.1716995115, 2018.
790 Gao, W., Fan, J., Easter, R. C., Yang, Q., Zhao, C., and Ghan, S. J.: Coupling spectral-bin cloud
791   microphysics with the MOSAIC aerosol model in WRF-Chem: Methodology and results for
792   marine stratocumulus clouds, J. Adv. Model. Earth Syst., 8, 1289–1309,
793   https://doi.org/10.1002/2016MS000676.Received, 2016.

794   Geerts, B., Miao, Q., Yang, Y., Rasmussen, R., and Breed, D.: An Airborne Profiling Radar
795   Study of the Impact of Glaciogenic Cloud Seeding on Snowfall from Winter Orographic
796   Clouds, J. Atmos. Sci., 67, 3286–3302, https://doi.org/10.1175/2010JAS3496.1, 2010.
797   Glienke, S. and Mei, F.: Two-Dimensional Stereo (2D-S) Probe Instrument Handbook. Ed. by
798   Robert Stafford, ARM user facility. DOE/SC-ARM-TR-233. 10.2172/1597436, 2019.
799   Glienke, S. and Mei, F.: Fast Cloud Droplet Probe (FCDP) Instrument Handbook. Ed. by Robert
800   Stafford, ARM user facility. DOE/SC-ARM-TR-238. 10.2172/1597469, 2020.
801   Goldberger, L. A.: Passive Cavity Aerosol Spectrometer Probe Aboard Aircraft (PCASP-AIR)
802   with Signal Processing Package 200 Instrument Handbook. Ed. by Robert Stafford, ARM
803   user facility. DOE/SC-ARM-TR-241, 2020.
804   Gong, S. L., Barrie, L. A., and Blanchet, J. P.: Modeling sea-salt aerosols in the atmosphere 1.
805   Model development, J. Geophys. Res.-Atmo., 102, 3805–3818,
806   https://doi.org/10.1029/96jd02953, 1997a.
807   Gong, S. L., Barrie, L. A., Prospero, J. M., Savoie, D. L., Ayers, G. P., Blanchet, J. P., and
808   Spacek, L.: Modeling sea-salt aerosols in the atmosphere 2. Atmospheric concentrations and
809   fluxes, J. Geophys. Res.-Atmo., 102, 3819–3830, https://doi.org/10.1029/96jd03401, 1997b.
810   Gourley, J., B. Kaney, and Maddox R.: Evaluating the calibrations of radars: A software
811   approach. Preprints, 31st Int. Conf. on Radar Meteorology, Seattle, WA, Amer. Meteor.
812   Soc., 459–462, 2003.
813   Gourley, J. J., Illingworth, A. J., and Tabary, P: Absolute Calibration of Radar Reflectivity Using
814   Redundancy of the Polarization Observations and Implied Constraints on Drop Shapes, J.
815   Atmos. Ocean Technol., 26(4), 689-703, 2009
816   Guenther, A. B., Jiang, X., Heald, C. L., Sakulyanontvittaya, T., Duhl, T., Emmons, L. K., and
817   Wang, X.: The Model of Emissions of Gases and Aerosols from Nature version 2.1
818   (MEGAN2.1): an extended and updated framework for modeling biogenic emissions,
819   Geosci. Model Dev., 5, 1471–1492, https://doi.org/https://doi.org/10.5194/gmd-5-1471-
820   2012, 2012.
821   Hazra, A., Padmakumari, B., Maheskumar, R. S., and Chen, J. P.: The effect of mineral dust and
822   soot aerosols on ice microphysics near the foothills of the Himalayas: A numerical
823   investigation, Atmos. Res., 171, 41–55, https://doi.org/10.1016/j.atmosres.2015.12.005,
824   2016.
825   Helmus, J. J. and Collis, S. M.: The Python ARM Radar Toolkit (Py-ART), a library for working
826   with weather radar data in the Python programming language, J. Open Res. Software, 4,
827   e25, https://doi.org/10.5334/jors.119, 2016
828   Hoose, C., Kristjánsson, J. E., and Burrows, S. M.: How important is biological ice nucleation in
829   clouds on a global scale?, Environ. Res. Lett., 5, 24009, https://doi.org/10.1088/1748-
830   9326/5/2/024009, 2010.
831   Iacono, M. J., Delamere, J. S., Mlawer, E. J., Shephard, M. W., Clough, S. A., and Collins, W.
832   D.: Radiative forcing by long-lived greenhouse gases: Calculations with the AER radiative
833   transfer models, J. Geophys. Res.-Atmo., 113,
834   https://doi.org/https://doi.org/10.1029/2008jd009944, 2008.
835   Janjić, Z. I. and Prediction, N. C. for E.: Nonsingular implementation of the Mellor-Yamada
836   level 2.5 scheme in the NCEP Meso model, 2001.
837   Kanji, Z. A., Ladino, L. A., Wex, H., Boose, Y., Burkert-Kohn, M., Cziczo, D. J., and Krämer,
838   M.: Overview of Ice Nucleating Particles, Meteorol. Monogr. 58, 1.1-1.33,
839   https://doi.org/10.1175/amsmonographs-d-16-0006.1, 2017.

840 Khain, A., Lynn, B., and Dudhia, J.: Aerosol Effects on Intensity of Landfalling Hurricanes as
841   Seen from Simulations with the WRF Model with Spectral Bin Microphysics, J. Atmos.
842   Sci., 67, 365–384, https://doi.org/doi:10.1175/2009JAS3210.1, 2010.
843 Khain, A. P., Leung, L. R., Lynn, B., and Ghan, S.: Effects of aerosols on the dynamics and
844   microphysics of squall lines simulated by spectral bin and bulk parameterization schemes, J.
845   Geophys. Res.-Atmo., 114, https://doi.org/10.1029/2009jd011902, 2009.
846 Korolev, A. v, Isaac, G. A., Cober, S. G., Strapp, J. W., and Hallett, J.: Microphysical
847   characterization of mixed-phase clouds, Q. J. Roy. Meteorol. Soc., 129, 39–65,
848   https://doi.org/https://doi.org/10.1256/qj.01.204, 2003.
849 Letcher, T., Cotton, W.R., 2014. The effect of pollution aerosol on wintertime orographic
850   precipitation in the Colorado Rockies using a simplified emissions scheme to predict CCN
851   concentrations, J. Appl. Meteorol. Climatol. 53 (4), 859–872.
852 Levin, E. J. T., DeMott, P. J., Suski, K. J., Boose, Y., Hill, T. C. J., McCluskey, C. S., Schill, G.
853   P., Rocci, K., Al-Mashat, H., Kristensen, L. J., Cornwell, G., Prather, K., Tomlinson, J.,
854   Mei, F., Hubbe, J., Pekour, M., Sullivan, R., Leung, L. R., and Kreidenweis, S. M.:
855   Characteristics of Ice Nucleating Particles in and Around California Winter Storms, J.
856   Geophys. Res.-Atmo., 124, 11530–11551, https://doi.org/10.1029/2019JD030831, 2019.
857 Lin, Y., Fan, J., Jeong, J.-H., Zhang, Y., Homeyer, C. R., and Wang, J.: Urbanization-Induced
858   Land and Aerosol Impacts on Storm Propagation and Hail Characteristics, J. Atmos. Sci.,
859   78, 925–947, https://doi.org/10.1175/jas-d-20-0106.1, 2020.
860 Martin, A. C., Cornwell, G., Beall, C. M., Cannon, F., Reilly, S., Schaap, B., Lucero, D.,
861   Creamean, J., Martin Ralph, F., Mix, H. T., and Prather, K.: Contrasting local and long-
862   range-transported warm ice-nucleating particles during an atmospheric river in coastal
863   California, USA, Atmos. Chem. Phys., 19, 4193–4210, https://doi.org/10.5194/acp-19-
864   4193-2019, 2019.
865 Matthews, A., F. Mei, and Comstock, J.: Water content monitor (WCM-2000), ARM Airborne
866   Facility (AAF). Atmospheric Radiation Measurement (ARM) Climate Research Facility
867   Data Archive, data set acquired 27 Jan 2015 and accessed 10 Jan 2016, 2015.
868 McCluskey, C. S., Ovadnevaite, J., Rinaldi, M., Atkinson, J., Belosi, F., Ceburnis, D., Marullo,
869   S., Hill, T. C. J., Lohmann, U., Kanji, Z. A., O'Dowd, C., Kreidenweis, S. M., and DeMott,
870   P. J.: Marine and Terrestrial Organic Ice-Nucleating Particles in Pristine Marine to
871   Continentally Influenced Northeast Atlantic Air Masses, J. Geophys. Res.-Atmo., 123,
872   6196–6212, https://doi.org/10.1029/2017JD028033, 2018a.
873 McCluskey, C. S., Hill, T. C. J., Humphries, R. S., Rauker, A. M., Moreau, S., Strutton, P. G.,
874   Chambers, S. D., Williams, A. G., McRobert, I., Ward, J., Keywood, M. D., Harnwell, J.,
875   Ponsonby, W., Loh, Z. M., Krummel, P. B., Protat, A., Kreidenweis, S. M., and DeMott, P.
876   J.: Observations of Ice Nucleating Particles Over Southern Ocean Waters, Geophys. Res.
877   Lett., 45, 11,989-11,997, https://doi.org/10.1029/2018GL079981, 2018b.
878 Mellor, G. L. and Yamada, T.: Development of a turbulence closure model for geophysical fluid
879   problems, Rev. Geophys., 20, 851–875,
880   https://doi.org/https://doi.org/10.1029/RG020i004p00851, 1982.
881 Meyers, M. P., DeMott, P. J., and Cotton, W. R.: New Primary Ice-Nucleation Parameterizations
882   in an Explicit Cloud Model, J. Appl. Meteorol., 31, 708–721, https://doi.org/10.1175/1520-
883   0450(1992)031<0708:NPINPI>2.0.CO;2, 1992.

884   Muhlbauer, A., Lohmann, U.: Sensitivity studies of the role of aerosols in warm- phase
885   orographic precipitation in different dynamical flow regimes. J. Atmos. Sci. 65 (8), 2522–
886   2542, 2008.
887   Muhlbauer, A. and Lohmann, U.: Sensitivity studies of aerosol-cloud interactions in mixed-
888   phase orographic precipitation, J. Atmos. Sci., 66, 2517–2538,
889   https://doi.org/10.1175/2009JAS3001.1, 2009.
890   Murray, B. J., O'Sullivan, D., Atkinson, J. D., and Webb, M. E.: Ice nucleation by particles
891   immersed in supercooled cloud droplets, Chem. Soc. Rev., 41, 6519–6554,
892   https://doi.org/10.1039/c2cs35200a, 2012.
893   Niemand, M., Möhler, O., Vogel, B., Vogel, H., Hoose, C., Connolly, P., Klein, H., Bingemer,
894   H., DeMott, P., Skrotzki, J., and Leisner, T.: A Particle-Surface-Area-Based
895   Parameterization of Immersion Freezing on Desert Dust Particles, J. Atmos. Sci., 69, 3077–
896   3092, https://doi.org/10.1175/jas-d-11-0249.1, 2012.
897   Ralph, F. M., Prather, K. A., Cayan, D., Spackman, J. R., DeMott, P., Dettinger, M., Fairall, C.,
898   Leung, R., Rosenfeld, D., Rutledge, S., Waliser, D., White, A. B., Cordeira, J., Martin, A.,
899   Helly, J., and Intrieri, J.: CalWater Field Studies Designed to Quantify the Roles of
900   Atmospheric Rivers and Aerosols in Modulating U.S. West Coast Precipitation in a
901   Changing Climate, Bull. Am. Meteorol. Soc., 97, 1209–1228, https://doi.org/10.1175/bams-
902   d-14-00043.1, 2016.
903   Reynolds, D. W.: A Report on Winter Snowpack-Augmentation, Bull. Am. Meteorol. Soc., 69,
904   1290–1300, https://doi.org/10.1175/1520-0477(1988)069<1290:AROWSA>2.0.CO;2, 1988.
905   Rosenfeld, D., Chemke, R., Demott, P., Sullivan, R. C., Rasmussen, R., McDonough, F.,
906   Comstock, J., Schmid, B., Tomlinson, J., Jonsson, H., Suski, K., Cazorla, A., and Prather,
907   K.: The common occurrence of highly supercooled drizzle and rain near the coastal regions
908   of the western United States, J. Geophys. Res.-Atmo., 118, 9819–9833,
909   https://doi.org/10.1002/jgrd.50529, 2013.
910   Saleeby, S.M., Cotton, W.R., Fuller, J.D.: The cumulative impact of cloud droplet nucleating
911   aerosols on orographic snowfall in Colorado, J. Appl. Meteorol. Climatol. 50 (3), 604–625,
912   2011.
913   Saleeby, S.M., Cotton, W.R., Lowenthal, D., Messina, J.: Aerosol impacts on the microphysical
914   growth processes of orographic snowfall. J. Appl. Meteorol. Climatol. 52 (4), 834–852,
915   2013.
916   Schmid, B., Tomlinson, J. M., Hubbe, J. M., Comstock, J. M., Mei, F., Chand, D., Pekour, M. S.,
917   Kluzek, C. D., Andrews, E., Biraud, S. C., and McFarquhar, G. M.: The DOE arm aerial
918   facility, Bull. Am. Meteorol. Soc., 95, 723–742, https://doi.org/10.1175/BAMS-D-13-
919   00040.1, 2014.
920   Shaw, W. J., Jerry Allwine, K., Fritz, B. G., Rutz, F. C., Rishel, J. P., and Chapman, E. G.: An
921   evaluation of the wind erosion module in DUSTRAN, Atmos. Environ., 42, 1907–1921,
922   https://doi.org/10.1016/j.atmosenv.2007.11.022, 2008.
923   Simmel, M. and Wurzler, S.: Condensation and activation in sectional cloud microphysical
924   models, Atmos. Res., 80, 218-236, 10.1016/j.atmosres.2005.08.002, 2006.
925   Thompson, D. R., McCubbin, I., Gao, B. C., Green, R. O., Matthews, A. A., Mei, F., Meyer, K.
926   G., Platnick, S., Schmid, B., Tomlinson, J., and Wilcox, E.: Measuring cloud
927   thermodynamic phase with shortwave infrared imaging spectroscopy, J. Geophys. Res.-
928   Atmo., 121, 9174–9190, https://doi.org/10.1002/2016JD024999, 2016.

Uin, J.: Ultra-High-Sensitivity Aerosol Spectrometer (UHSAS) Instrument Handbook. Ed. by
    Robert Stafford, DOE ARM Climate Research Facility. DOE/SC-ARM-TR-163, 2016.

Uno, I., Eguchi, K., Yumimoto, K., Takemura, T., Shimizu, A., Uematsu, M., Liu, Z., Wang, Z.,
    Hara, Y., and Sugimoto, N.: Asian dust transported one full circuit around the globe, Nat.
    Geosci., 2, 557–560, https://doi.org/10.1038/ngeo583, 2009.

Vali, G., DeMott, P. J., Möhler, O., and Whale, T. F.: Technical Note: A proposal for ice
    nucleation terminology, Atmos. Chem. Phys., 15, 10263–10270,
    https://doi.org/10.5194/acp-15-10263-2015, 2015.

Vergara-Temprado, J., Murray, B. J., Wilson, T. W., O'Sullivan, D., Browse, J., Pringle, K. J.,
    Ardon-Dryer, K., Bertram, A. K., Burrows, S. M., Ceburnis, D., Demott, P. J., Mason, R.
    H., O'Dowd, C. D., Rinaldi, M., and Carslaw, K. S.: Contribution of feldspar and marine
    organic aerosols to global ice nucleating particle concentrations, Atmos. Chem. Phys., 17,
    3637–3658, https://doi.org/10.5194/acp-17-3637-2017, 2017.

Xiao, H., Yin, Y., Jin, L., Chen, Q., and Chen, J.: Simulation of the effects of aerosol on mixed-
    phase orographic clouds using the WRF model with a detailed bin microphysics scheme,
    Atmos. Sci. Lett., 120, 8345–8358, https://doi.org/https://doi.org/10.1002/2014JD022988,
    2015.

Xue, L., Fan, J., Lebo, Z. et al.: Idealized Simulations of a Squall Line from the MC3E Field
    Campaign Applying Three Bin Microphysics Schemes: Dynamic and Thermodynamic
    Structure, Mon. Wea. Rev., 145, 4789- 4812, https://doi.org/10.1175/MWR-D-16-0385.1,
    2017.

Yang, Y., Sun, J., Zhu, Y., and Zhang, T.: Examination of the impacts of ice nuclei aerosol
    particles on microphysics, precipitation and electrification in a 1.5D aerosol-cloud bin
    model, J. Aerosol Sci., 140, 105440, https://doi.org/10.1016/j.jaerosci.2019.105440, 2020.

Yun, Y. and Penner, J. E.: An evaluation of the potential radiative forcing and climatic impact of
    marine organic aerosols as heterogeneous ice nuclei, Geophys. Res. Lett., 40, 4121–4126,
    https://doi.org/10.1002/grl.50794, 2013.

Zaveri, R. A., Easter, R. C., Fast, J. D., and Peters, L. K.: Model for Simulating Aerosol
    Interactions and Chemistry (MOSAIC), J. Geophys. Res.-Atmo., 113,
    https://doi.org/https://doi.org/10.1029/2007jd008782, 2008.

Zhang, Y., Fan, J., Li, Z., and Rosenfeld, D.: Impacts of Cloud Microphysics Parameterizations
    on Simulated Aerosol–Cloud-Interactions for Deep Convective Clouds over Houston,
    Atmos. Chem. Phys., 1–46, https://doi.org/10.5194/acp-2020-372, 2020.

Zhao, B., Wang, Y., Gu,Y., Liou, K.-N., Jiang, J. H., Fan, J., Liu, X., Huang, L., and Yung, Y.
    L.: Ice nucleation by aerosols from anthropogenic pollution, Nature Geosciences, 12,
    https://doi.org/10.1038/s41561-019-0389-4, 2019.

Zhao, C., Chen, S., Leung, L. R., Qian, Y., Kok, J. F., Zaveri, R. A., and Huang, J.: Uncertainty
    in modeling dust mass balance and radiative forcing from size parameterization, Atmos.
    Chem. Phys., 13, 10733–10753, https://doi.org/10.5194/acp-13-10733-2013, 2013

970   **Figures**
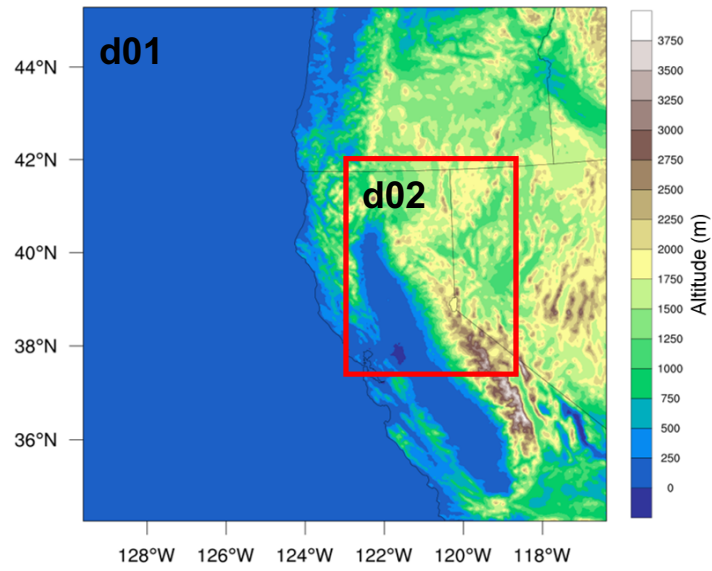
971

972   **Figure 1.** Two nested simulation domains: d01 and d02 centering over California. The color

973   shading denotes the terrain elevation.

974
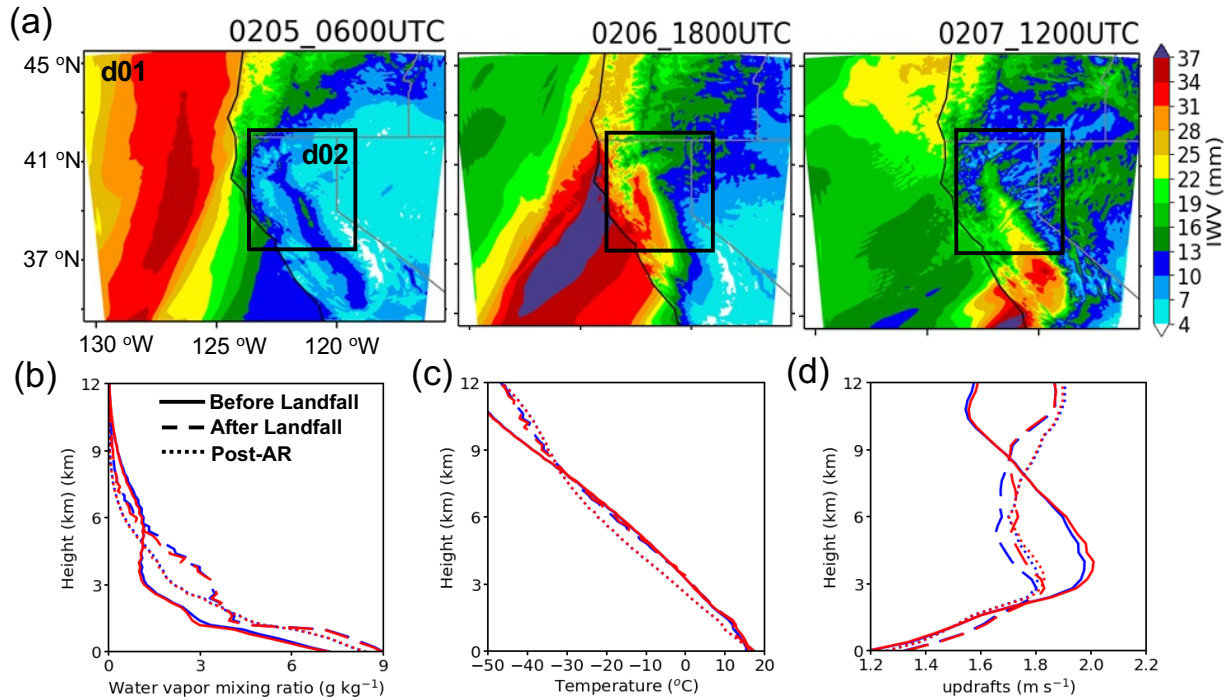
Figure 2. (a) Evolution of integrated water vapor (IWV) at 06:00 UTC 5 February (before AR landfall), 18:00 UTC 6 February (after AR landfall), and 12:00 UTC 7 February (post-AR). The black box (i.e., d02) in (a) is the domain of this study with the 5 lateral boundary grids excluded for analysis at each side. (b-d) show the mean vertical profiles of (b) water vapor mixing ratio, (c) temperature, and (d) updraft velocity at the three AR stages, i.e., before (solid lines) and after (dashed lines) AR landfall and post-AR stages (dotted lines), for the simulations of DM15 (blue) and DM15+MC18 (red). The water vapor mixing ratio and temperature are averaged for cloud-free grids, and updraft velocity is averaged over the grids with a vertical velocity greater than 1 m s^{-1}.
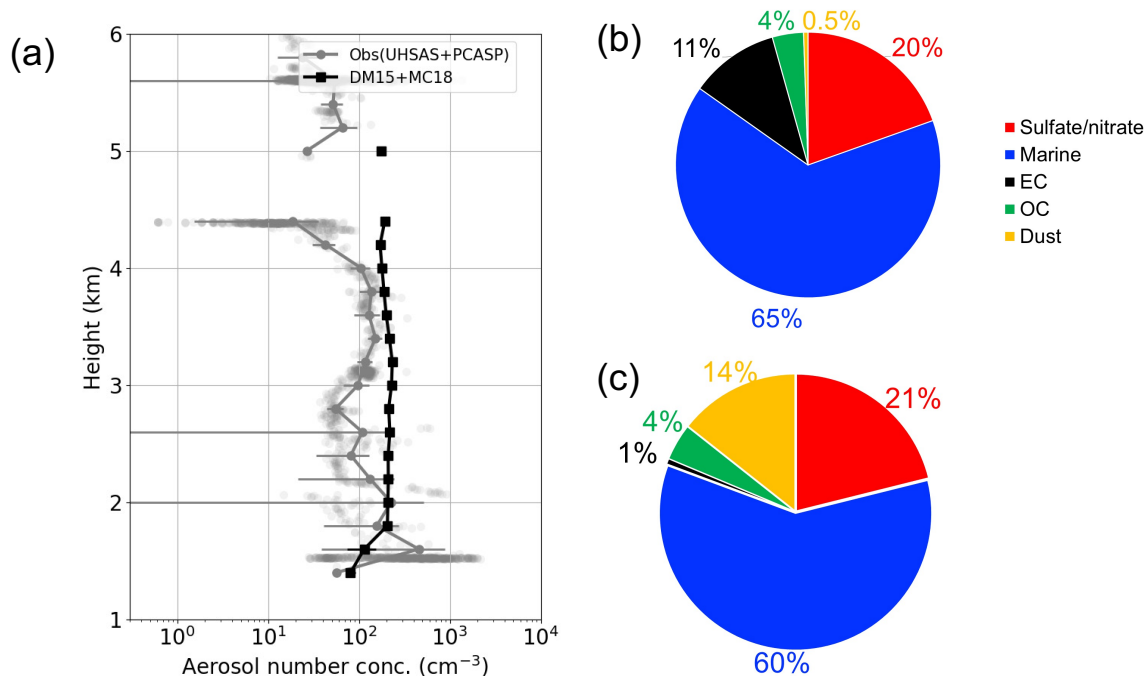
Figure 3. (a) Vertical distributions of aerosol number concentrations from aircraft observations (Obs, grey) and DM15+MC18 (black) for particles with a dry diameter over a range of 0.067~3 μm, (b) mean fractional number contributions of aerosol classifications based on measurements of single-particle mass spectra of aerosols and cloud particle residuals reported in Levin et al. (2019), and (c) mean fractional mass contributions of aerosols in DM15+MC18 (number concentration for each aerosol component is not predicted by WRF-Chem). The aerosol number concentration from aircraft observations in (a) consists of both measurements from UHSAS and PCASP. The modeled data in (a) and (c) are sampled along the aircraft route on 7 February 2015.
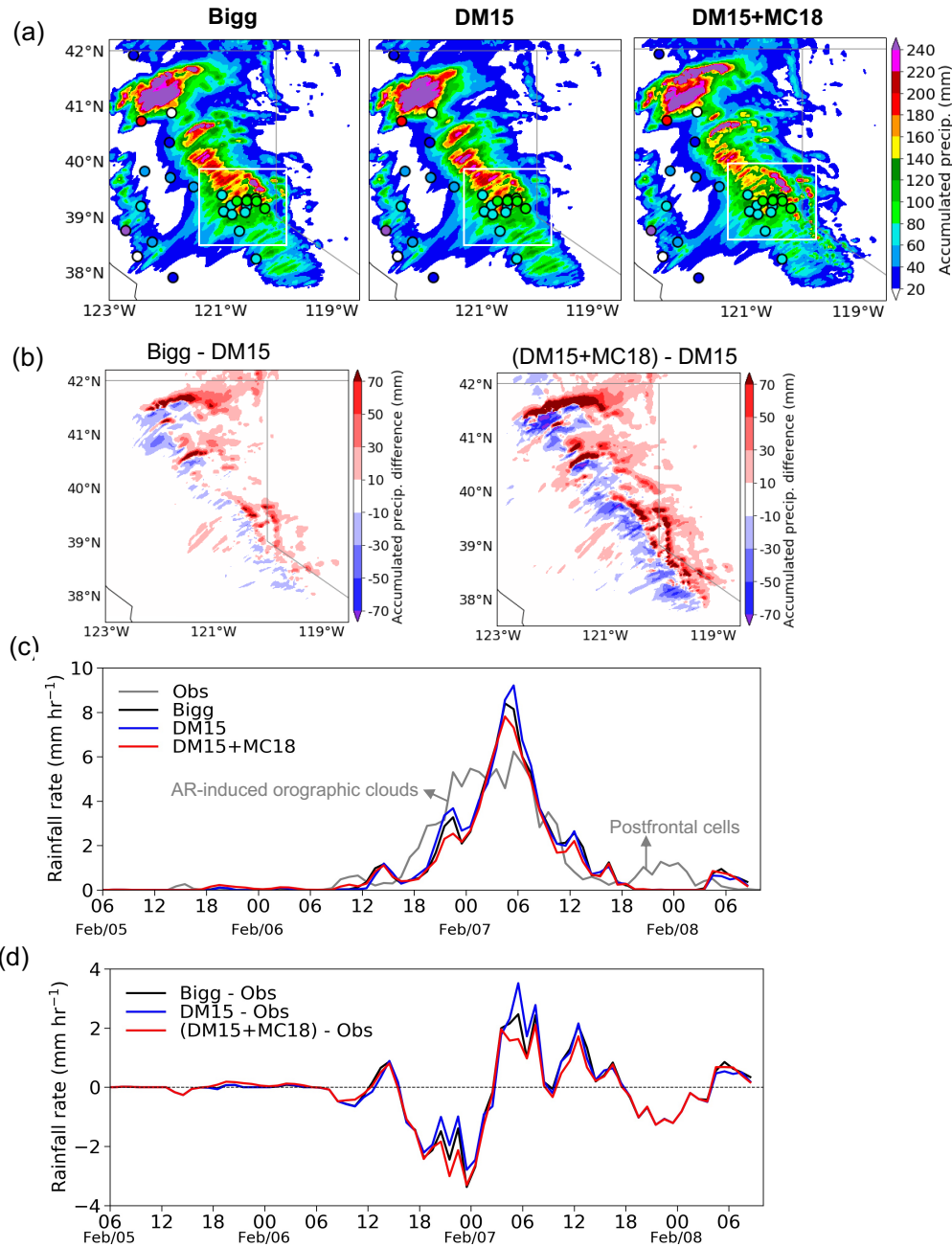
Figure 4. (a) Spatial distributions of accumulated precipitation during the AR event (5 Feb. 06:00 – 8 Feb. 09:00 UTC) from Bigg, DM15, and DM15+MC18. The color shading is for simulations and the circles denote the rain gauge measurements provided by NOAA Physical Sciences Laboratory. (b) as (a) but for differences between Bigg and DM15 (left) and between DM15+MC18 and DM15 (right). (c) Time series of precipitation rates during the entire AR event for rain gauge observations (grey line), Bigg (black line), DM15 (blue line), and DM15+MC18 (red line). (d) Differences between the simulations and observations based on the data of (b). The precipitation rates in (b) are averaged over all the rain gauge sites shown in (a). The white boxes in (a) mark the region where the precipitation simulation is improved by adding marine INPs.
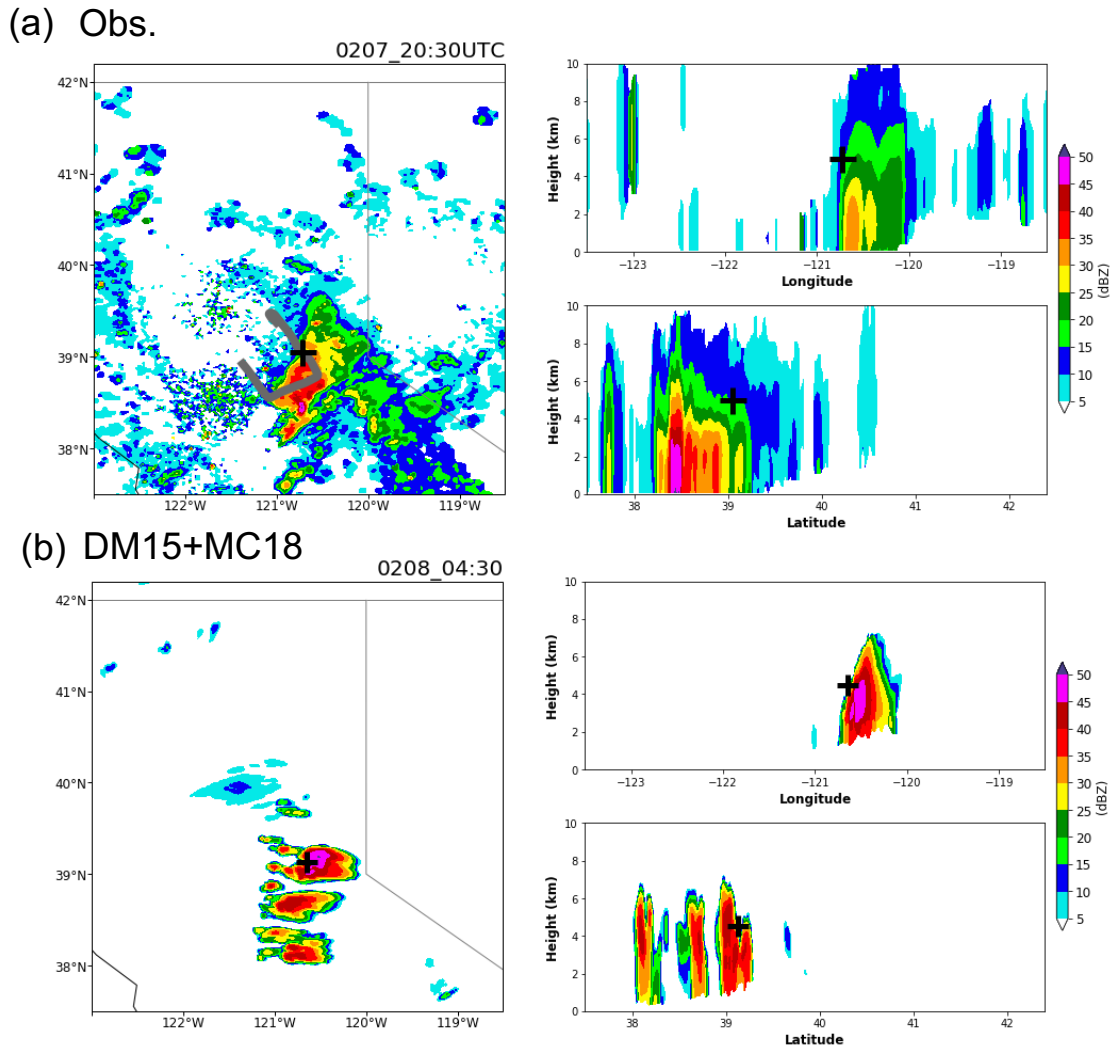
Figure 5. (a) Composite reflectivity of NEXRAD for the postfrontal clouds that the G-1 aircraft sampled, (b) composite reflectivity from the simulation of DM15+MC18 for the postfrontal clouds. The observation and simulation are compared at the peak reflectivity time which is 20:30 UTC 7 February for the observed clouds and 04:30 UTC 8 February for the simulated clouds. The black crosses in the left two panels denote the positions where the longitude-height and latitude-height cross-sections in the right panels are plotted. The grey line in the left panel of (a) shows the flight track of the G-1 aircraft.
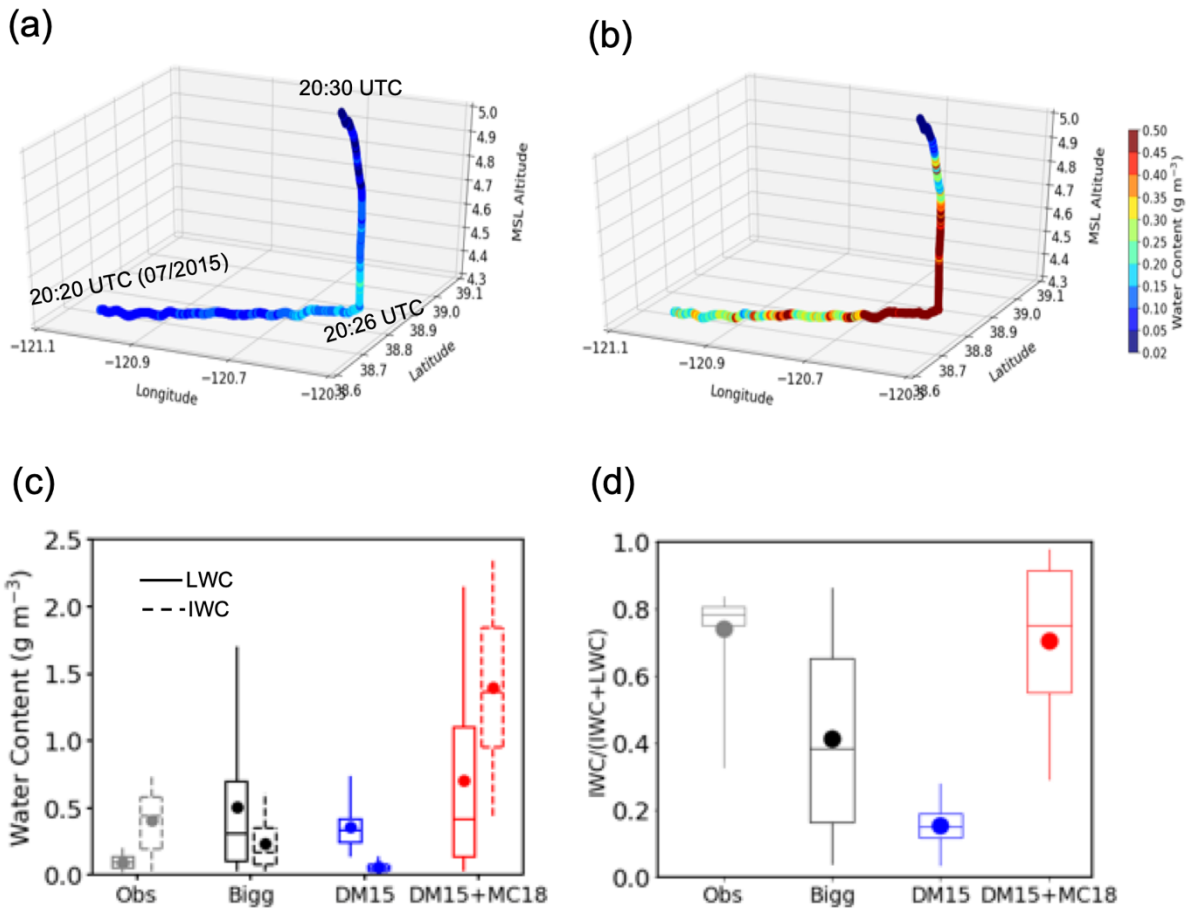
Figure 6. Comparisons of the simulations with aircraft observations. The observed (a) LWC and (b) IWC along the flight track during 20:20 – 20:30 on 7 February when the aircraft flew through the mixed-phase regime of the postfrontal clouds. (c) LWC (solid) and IWC (dashed) and (d) the glaciation ratios of IWC/(IWC+LWC) from the aircraft measurements (Obs, grey) and simulations of Bigg (black), DM15 (blue), and DM15+MC18 (red). The boxes show the 25th, median (horizontal lines in the box), and 75th percentiles of the data. The upper and lower whiskers show the 95th and 5th percentiles, respectively. The mean values are denoted by circles.
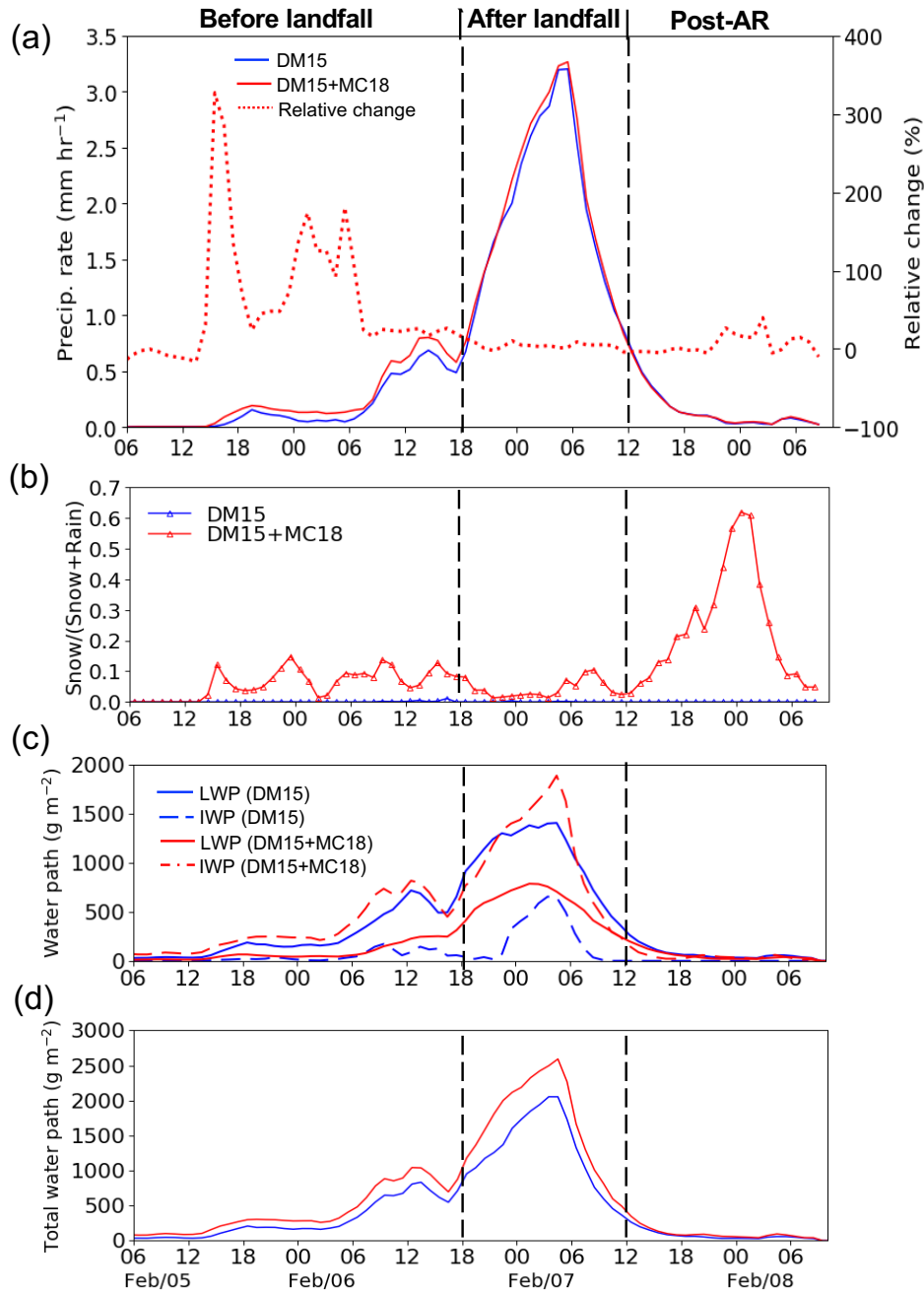
1024

1025 **Figure 7.** Time series of (a) precipitation rate (solid lines, left y-axis), (b) ratio of snow

1026 precipitation (i.e., snow/(snow+rain) in mass mixing ratio) at the lowest model level, (c) LWP

1027 (solid) and IWP (dashed) for DM15 (blue) and DM15+MC18 (red), and (d) total condensate

1028 water path (TWP). The relative changes in precipitation rate from DM15 to DM15+MC18 are

1029 shown in the red dotted line in (a) with values shown on the right y-axis. The vertical dashed

1030 lines divide the three AR stages.

1031

1032

Figure 8. Spatial distribution of accumulated precipitation during the stages of (a) before AR

landfall, (b) after AR landfall, and (c) post-AR in DM15 (left) and DM15+MC18 (right). The

parallelograms marked in (b) denotes the area for the east-west cross-section analysis shown in
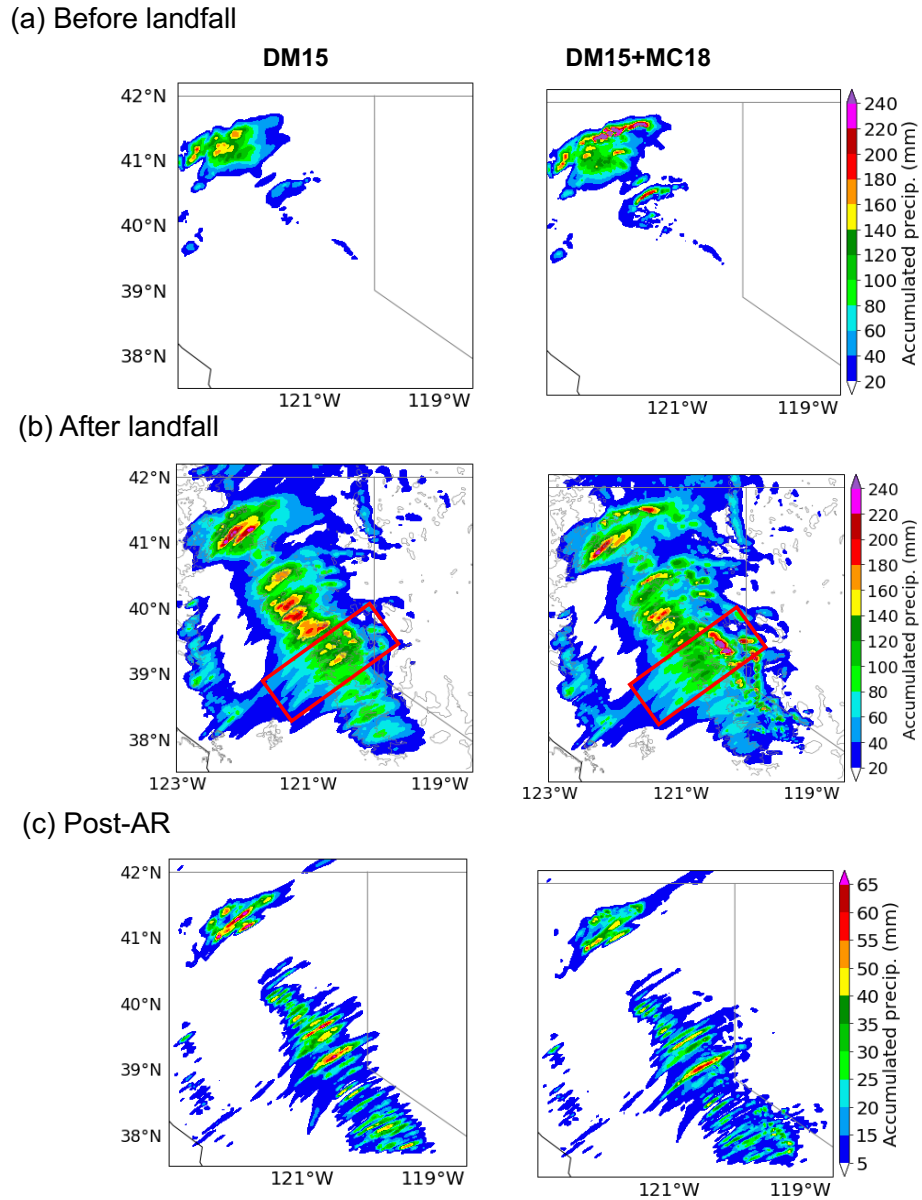
Figure 9.

1033

1034

1035

1036

1037

1038

1039
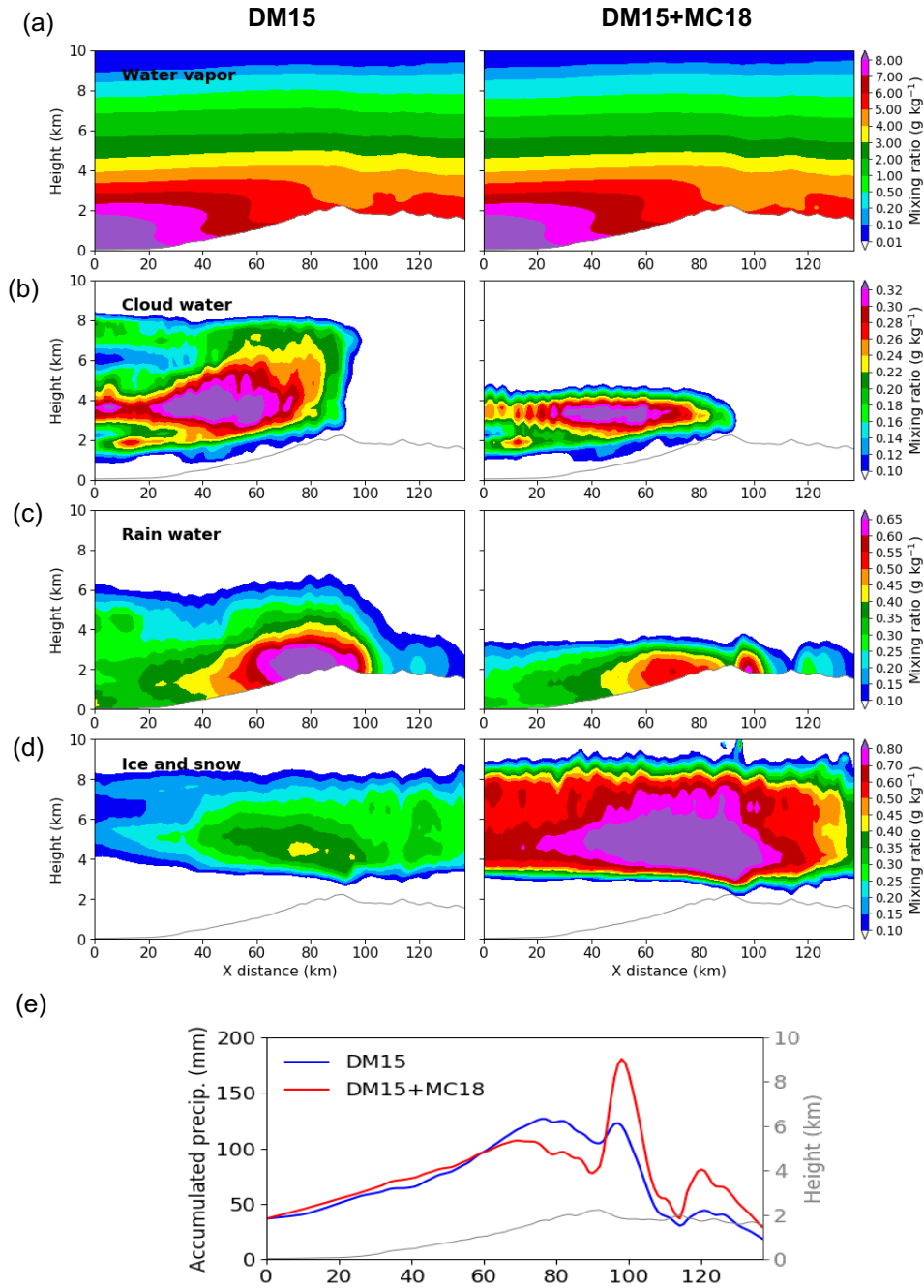
1040

1041

Figure 9. Mean mixing ratios of (a) water vapor, (b) cloud water, (c) rainwater, (d) ice + snow, and (e) surface precipitation at the stage after AR landfall in DM15 and DM15+MC18. The vertical cross-sections are averaged over the red boxes marked in Fig. 8b and the entire stage.

1045
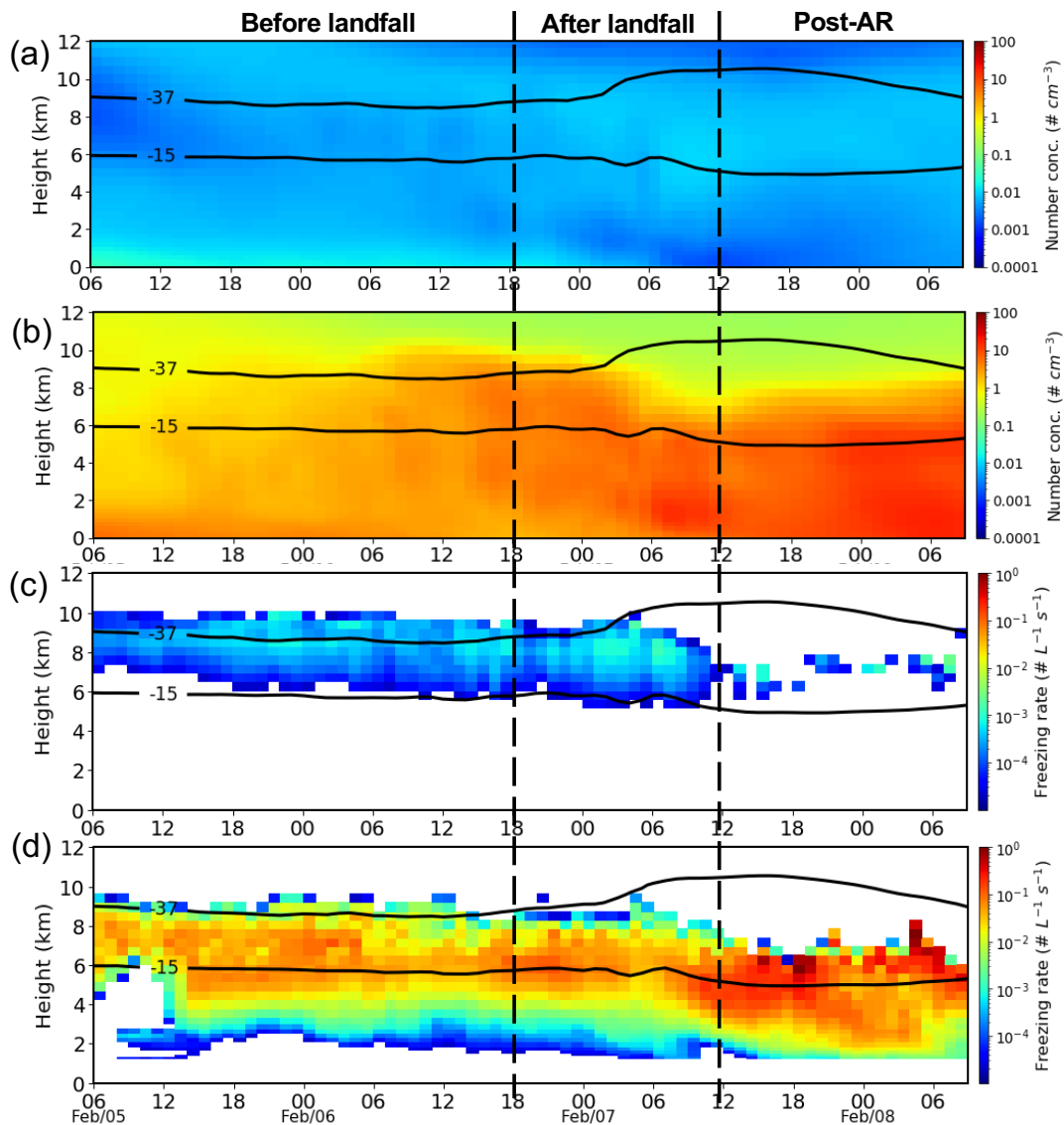
1046

1047   **Figure 10.** Time-height cross-sections of (a) dust particle (>0.5 μm) number concentration, (b)

1048   marine aerosol number concentration, (c) the freezing rate in DM15, and (d) the freezing rate in

1049   DM15+MC18. The number concentrations in (a) and (b) are derived from their corresponding

1050   mass mixing ratios under the clear-sky condition only. The freezing rates in (c) and (d) are the

1051   ice nucleation rates via immersion freezing at T > - 37 °C and the drop homogenous freezing

1052   rates at T < - 37 °C, and the values are for cloudy-points only. The black contour lines in each

1053   panel mark the temperature levels of -15 and -37 °C, representing the efficient immersion

1054   freezing temperature in DM15+MC18 and the homogeneous freezing temperature in the model,

1055   respectively.

1056
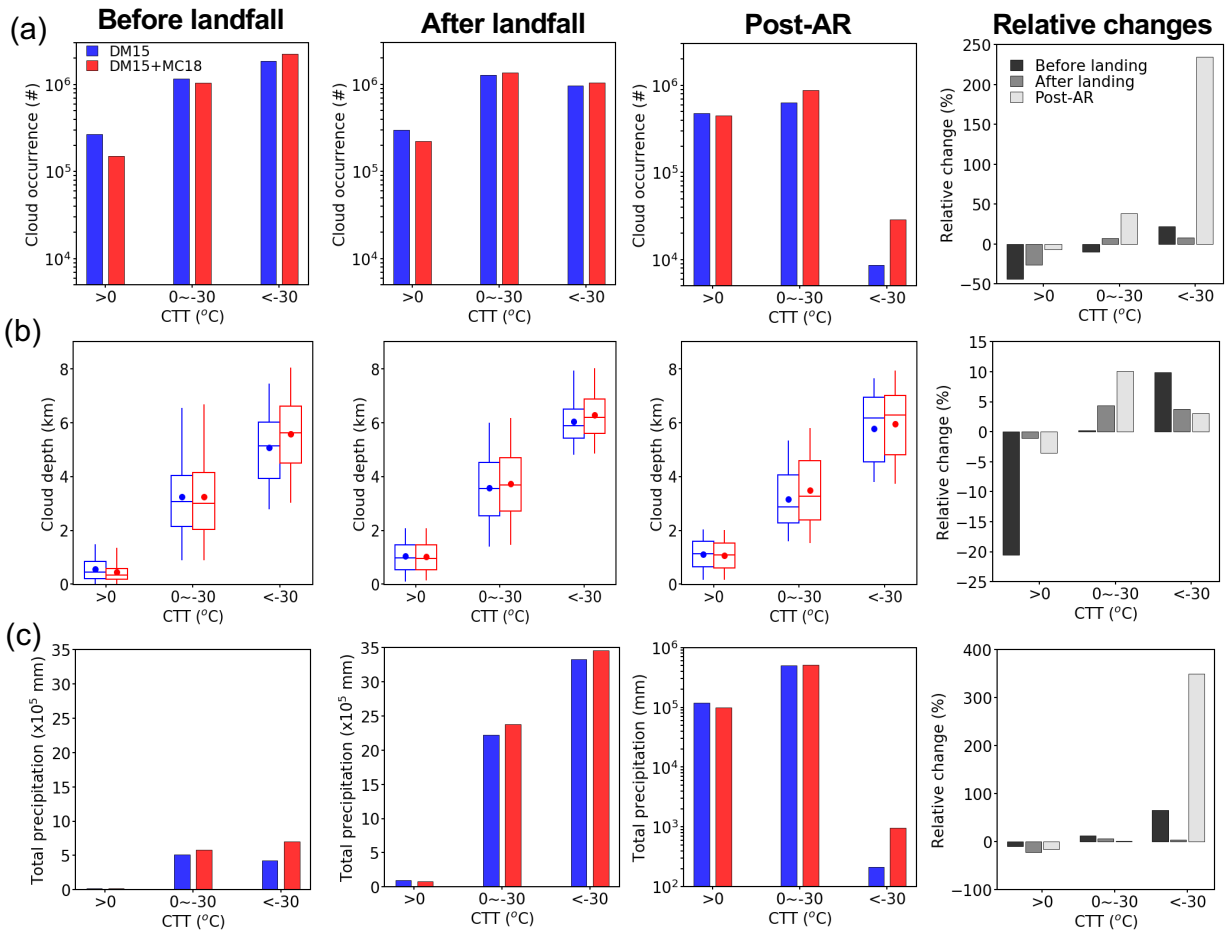
1057

1058 **Figure 11.** (a) Cloud occurrences, (b) cloud depth, and (c) total precipitation for three cloud

1059 regimes in DM15 (blue) and DM15+MC18 (red) at three AR stages from left to right: before AR

1060 landfall, after AR landfall, post-AR. The last column shows the relative changes caused by the

1061 marine INP effect, which are calculated as [(DM15+MC18) – DM15]/DM15*100%. Note that

1062 the total precipitation at the post-AR stage uses a log scale for the y-axis. The box-whisker plots

1063 follow the description in Figure 5c.
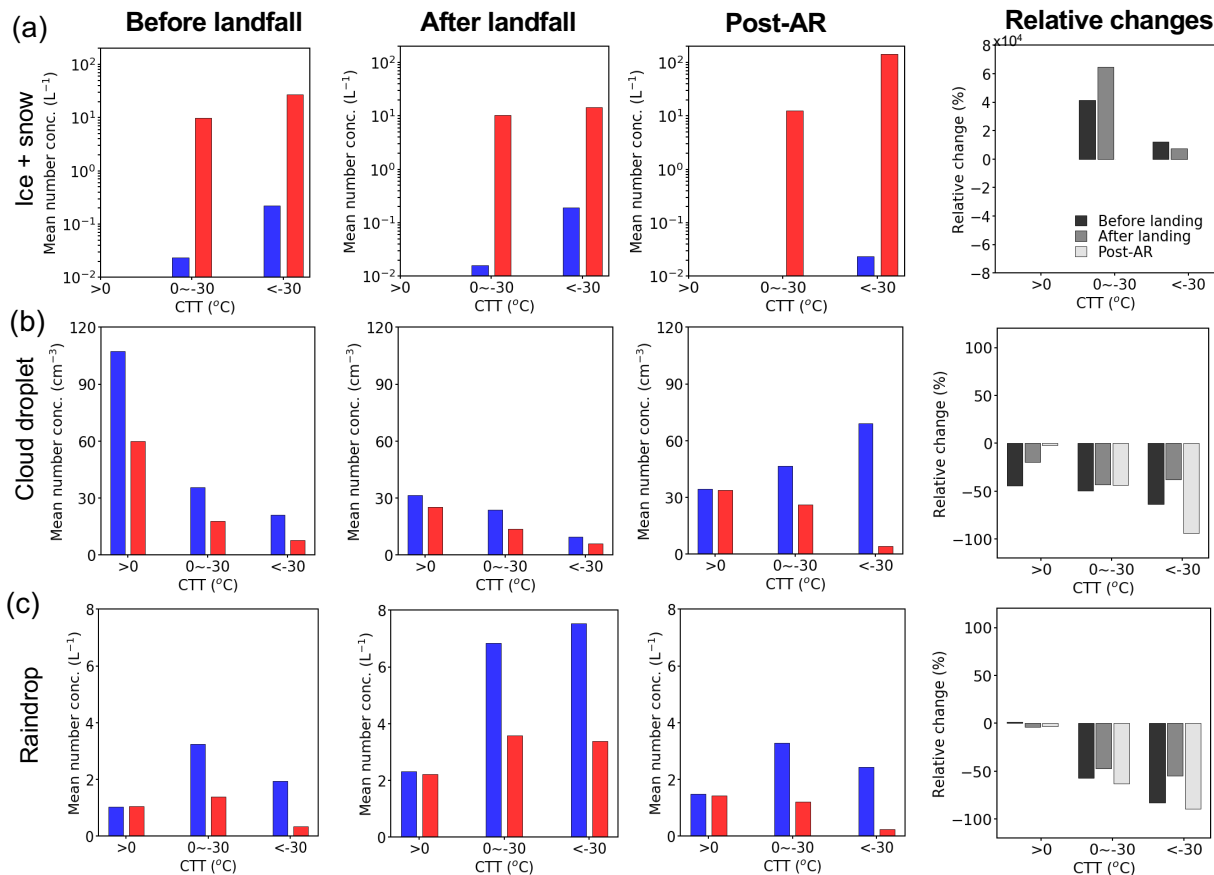
1064

Figure 12. Hydrometeor number concentrations and their relative changes in three cloud regimes

in DM15 (blue) and DM15+MC18 (red) at the three AR stages for (a) ice particles (sum of ice

and snow), (b) cloud droplets, and (c) raindrops. The last column shows the relative changes

caused by the marine INP effect, which are calculated as [(DM15+MC18) –

DM15]/DM15*100%. Since ice particles are very limited at the post-AR stage in DM15, the

percentage changes of ice particles from DM15 to DM15+MC18 are huge numbers that are

omitted from the plots.
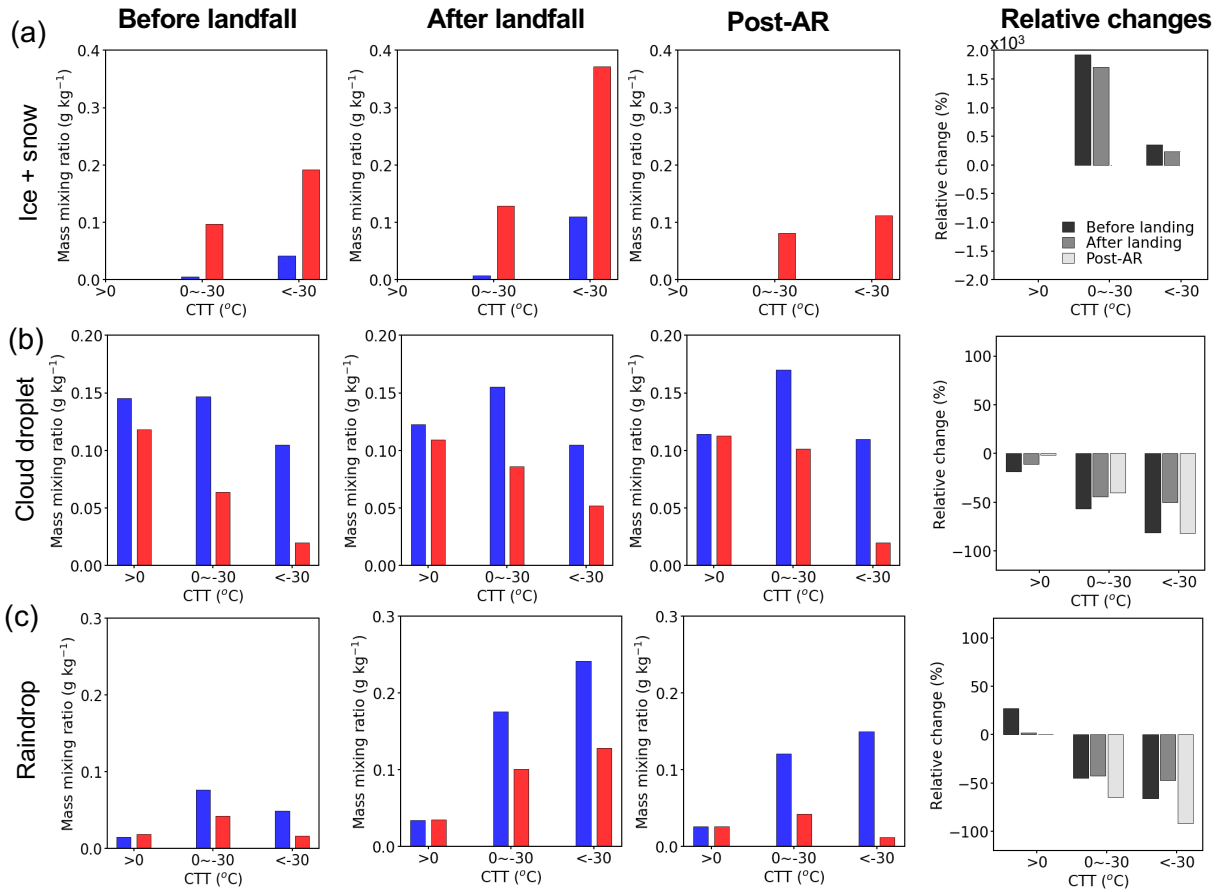
1072

1073 **Figure 13.** Same as Figure 12, except for the mass mixing ratios of (a) ice particles (sum of ice

1074 and snow), (b) cloud droplets, and (c) raindrops.

1075

1076

1077

1078

1079

1080

1081

1082

1083

1084

1085 **Table 1.** The changes in total precipitation, total condensate water path (TWP), liquid water path

1086 (LWP), and ice water path (IWP), and cloud fractions (CF), net cloud radiative forcing (CRF) at

1087 TOA from DM15 to DM15+MC18 (i.e., the marine INP effect), as well as the glaciation ratio,

1088 i.e., IWC/(LWC+IWC), and the ratios of snow precipitation, i.e., snow/(rain+snow) in mass

1089 mixing ratio at the lowest model level from DM15 to DM15+MC18, at the three AR stages. The

1090 percentage changes are calculated following ((DM15+MC18)- DM15)/DM15*100.

1091

AR stages		Before landfall	After landfall	Post-AR
Total precipitation		36%	4%	-1%
TWP		45%	29%	35%
LWP		-66%	-46%	-26%
IWP		8 times	5 times	440 times
CF		5%	4%	20%
Net CRF at TOA		15%	13%	10%
IWC/(LWC+IWC)	DM15	0.14	0.16	0.001
	DM15+MC18	0.74	0.59	0.36
Snow/(Rain+Snow)	DM15	0.002	0.001	<0.001
	DM15+MC18	0.085	0.042	0.131

1092

1093

1094 **Table 2.** The domain-mean mass rates of deposition and riming in the mixed-phase and deep

1095 cloud regimes in DM15 and DM15+MC18 at the three AR stages.

AR stages		Before landfall		After landfall		Post-AR	
		Mixed-phase clouds	Deep clouds	Mixed-phase clouds	Deep clouds	Mixed-phase clouds	Deep clouds
Deposition ($mg\ kg^{-1}\ h^{-1}$)	DM15	44	171	81	388	7	8
	DM15+MC18	846	780	1128	1397	781	1013
Riming ($mg\ kg^{-1}\ h^{-1}$)	DM15	27	89	57	297	25	34
	DM15+MC18	377	228	575	858	505	361

1096

1097